2013

Development of a Counter Rotating Vortex Pair (CVP) Mixer for Aerospace Applications

Jeongmoon Park
Purdue University, joshua1202@gmail.com

Graduate School ETD Form 9
(Revised 12/07)

PURDUE UNIVERSITY
GRADUATE SCHOOL
Thesis/Dissertation Acceptance

This is to certify that the thesis/dissertation prepared

By Jeongmoon Park

Entitled

Development of a Counter Rotating Vortex Pair (CVP) Mixer for Aerospace Applications

For the degree of Master of Science in Aeronautics and Astronautics

Is approved by the final examining committee:

Stephen D. Heister
Chair

Gregory A. Blaisdell

John P. Sullivan

To the best of my knowledge and as understood by the student in the *Research Integrity and Copyright Disclaimer (Graduate School Form 20)*, this thesis/dissertation adheres to the provisions of Purdue University's "Policy on Integrity in Research" and the use of copyrighted material.

Approved by Major Professor(s): Stephen D. Heister

Approved by: Marc H. Williams 11/13/2013
Head of the Graduate Program Date

DEVELOPMENT OF A COUNTER ROTATING VORTEX PAIR (CVP) MIXER FOR AEROSPACE APPLICATIONS

A Thesis

Submitted to the Faculty

of

Purdue University

by

Jeongmoon Park

In Partial Fulfillment of the

Requirements for the Degree

of

Master of Science in Aeronautics and Astronautics

December 2013

Purdue University

West Lafayette, Indiana

ACKNOWLEDGEMENTS

First and foremost, I praise and thank Jesus Christ for his guidance and giving me the best at all times. With the faith I have in Jesus, I look forward to the rest of my life that I will live for Him.

I would like to thank my wife, Yunyoung Kang, for her support, wisdom and love. Her sense of humor and wit always cheer me up and relieve my stress. I could never have done this without her dedication and sacrifice. She was the main reason that it was great at Purdue University. I also thank my son, Joshua J. Park, for being born healthy. Furthermore, there were strong support from my parents and parents in law. I greatly thank both parents for their help and all the prayers for me.

I would like to thank my chair advisory committee, Professor Stephen D. Heister, for his kindness, patience and continual help and advice. I esteem not only his knowledge but also his personality that treats students respectively. Thank him for giving me this great opportunity to work on this project. My advisory committee, Professor John P. Sullivan and Professor Gregory A. Blaisdell, all were pivotal in the development of the CVP mixer and evaluation of its

performances. Professor Gregory A. Blaisdell taught me potential theory that was the fundamental approach to the mixer design and Professor John P. Sullivan gave me useful guidance in the experiment and provided space for the test rig in the ASL. I greatly thank all my advisory committee for their supervision and constant help.

TABLE OF CONTENTS

Page

Page

LIST OF TABLE

LIST OF FIGURES

Figure Page

Figure Page

Figure Page

NOMENCLATURE

Acronyms

CVP	Counter rotating vortex pair
DMLS	Direct Metal Laser Sintering
ESP	Electronically Scanned Pressure Measurement

Symbols

a	Radius of a cylindrical boundary
dP	Static pressure drop
F	Complex potential
K	Loss coefficient
L	Total length of the CVP mixer
O	Center of a cylindrical boundary
q	Dynamic Pressure
r	Radial distance from a vortex center
R_R	Characteristic radius of the Rankine vortex
R_s	Radius of a ring support
u	x-direction /lateral velocity
v	y-direction/vertical velocity
v_α	Traverse velocity

v_θ	Tangential velocity
w	Axial velocity
W	Complex velocity potential
z	Axial distance
$z_{1\ (or\ 2)}$	Vortex center locations in the complex coordinate
$\overline{z}_{1\ (or\ 2)}$	Complex conjugate of $z_{1\ (or\ 2)}$
α	Local vane/swirl angle
α_i	Initial vane/swirl angle
α_{max}	Maximum vane/swirl angle
Γ	Vortex strength
Φ	Velocity potential
Ψ	Stream function

ABSTRACT

Park, Jeongmoon. M.S.A.A., Purdue University, December 2013. Development of a Counter Rotating Vortex Pair (CVP) Mixer for Aerospace Applications. Major Professor: Stephen Heister.

Swirling motions induced by a counter-rotating vortex pair (CVP) provides a mechanism to entrain fluid from the periphery of this structure and mix surrounding fluids with those within the vortex structure. Eventually, the vortices act upon each other transporting molecularly mixed fluid into the core flow. This mechanism has potential to increase efficiency with more complete mixing. Therefore, a mixer is proposed which directly induces counter rotating vortices by a three dimensional geometry. The proposed swirl mixer is designed to induce counter rotating vortices based on the potential flow theory, Milne-Thomson's Circle Theorem and Rankine vortex. Twelve test models are developed during the optimization process. Design factors were examined using a seven-hole pressure probe to investigate velocity vector fields produced by the test models, thereby obtaining an optimum CVP mixer that maximized tangential velocity with uniform axial flow. The optimized design was fabricated from Inconnel 718 using the Direct Metal Laser Sintering (DMLS) technology.

CHAPTER 1. INTRODUCTION

1.1 Mixing

Mixing problems are prevalent in many fields as industrial processes require mixing of liquids, combustors often require mixing of gases and liquids, and aerospace nozzles often require gas/gas mixing processes. Mixing can be promoted by turbulent processes, but there are numerous applications where the pressure drops to attain mixing must be minimized to enhance system performance. Gas-liquid systems enjoy the significant advantage afforded by atomization as it is an ideal process to disperse the liquid phase over substantial volumes of gas phase.

The volume of material on mixing problems is immense as there are so many practical applications over a wide number of industries. In this work, we focus on gas/gas mixer systems suitable for aerospace applications. In aerospace mixers, flow velocities tend to be high and losses from mixing can have substantial impact on system performance. Gas-gas mixers tend to be more challenging than gas/liquid systems as there are high volumetric flow rates for both fluids in

general. This is especially true in aerospace applications where velocities are high.

Entrainment of fluids in a turbulent mixing layer is the principal mechanism responsible for enhancing the mixing of two adjacent streams and the planar mixing layer remains a classical problem in fluid mechanics[1] . In general, shear layer-based mixing tends to be slow as compared to other alternatives, especially in high flow applications. Compressibility is known to inhibit mixing in shear layers and very high-speed flows, such as those in scramjet combustors face great challenges for this reason. A basic tenant for improving mixing of fluids is the creation of streamwise vorticity. Streamwise vortices provide swirling motions that effectively stir the fluids and a number of practical devices have been developed to exploit this phenomenon.

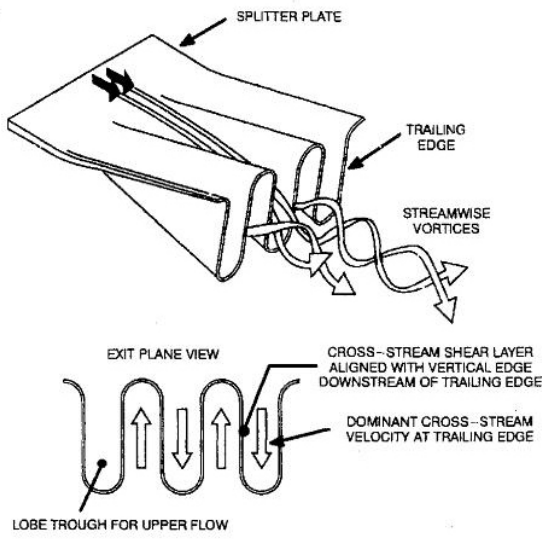

Figure 1.1 Schematic of the lobed mixer vertical structure, courtesy of McCormick[2]

The lobed mixer shown in Figure 1.1 is employed employed in many turbofan engine nozzles is a classic example. The velocity difference between the co-flowing streams, combined with the convoluted lobes generate streamwise vortices that develop into an array of counter rotating vortices, which are believed to be primarily responsible for the enhanced mixing[2]. A pair of counter rotating axial vortices stirs the field and a large amount of surrounding fluid is trapped by the engulfing surface. Eventually, the vortices act upon each other transporting molecularly mixed fluid into the core flow. This mechanism has potential to increase efficiency with more complete mixing. Therefore, a mixer is proposed which directly induces counter rotating vortices by a three dimensional geometry.

1.2 Counter-rotating Vortex Pair(CPV) Mixer Applications

The present work is preceded by some recent studies employing counter-rotating vortex pairs (CVP) to promote mixing of gaseous streams. Figure 1.2 provides a schematic of the streamlines produced in a CVP flow and the subsequent mixing process induced. In gas turbine applications, rapid mixing of hot engine exhaust with cool ambient air provides a mechanism for reducing infrared signatures of aircraft and improving survivability to a variety of threats from IR-guided missiles[8].

Tang[8] studied an unconventional 2-D nozzle and verified that the 2-D nozzle performed with increased efficiency and better mixing with a 20 degree single swirler. Based on Tang's research data, Luk[14] investigated the effects of a dual

swirling flow on the performance of the 2-D transitional nozzle. Luk found that his 30 degree dual swirler greatly enhanced the rate of dissipation in the plume.

The present work is motivated by the hybrid rocket engine as a potential application. Hybrid rockets employ gaseous oxidizers (or liquids that have been vaporized by the local flame zone) and a solid fuel. The mixing of the fuel vapors and the oxidizer is diffusion controlled and is typically quite slow at high velocity port conditions. The CVP approach has potential to stir unburned gaseous fuel into the center of the port that contains almost pure oxidizer and in doing so enhance combustion efficiency.

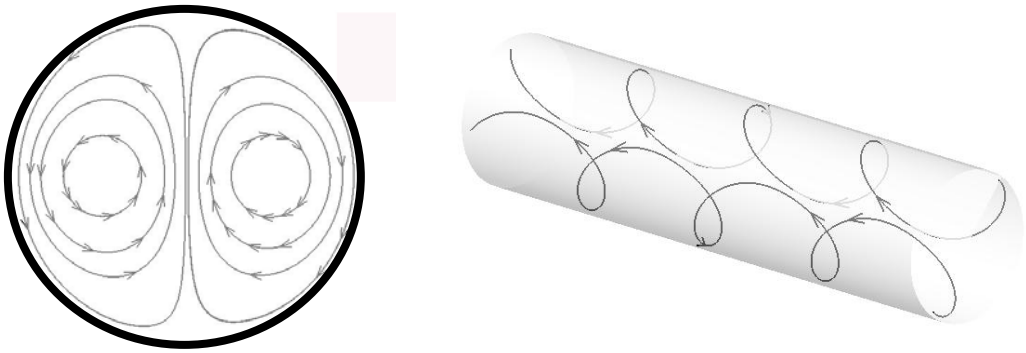

Figure 1.2 Schematic of vortex structure of a counter rotating vortex pair in a cylindrical solid boundary in 2D and 3D

One of the solutions of this significant disadvantage that many researchers have been focused on is to modify of flow characteristics by inducing swirls in the oxidizer flow. A swirling flow field in the combustion chamber provides the additional tangential velocity near the fuel surface, and increases convective heat transfer. As a result, the regression rate is augmented by the enhanced heat

flux[1,2]. Furthermore, the centrifugal force due to the swirling flow also has favorable effects by increasing the pressure on the fuel surface and the swirling increases the residence time of combustion gas in the chamber, causing the combustion efficiency of the hybrid engine to increase.

Knuth et al studied a technique of applying swirl to an oxidizer injection flow to improve the combustion property of hybrid combustion. He found that the hybrid injected by the proposed technique exhibited regression rates 4 to 8.4 times higher than a conventional head end injected hybrid at a comparable oxidizer mass flux[1]. This work also confirmed that fuel regression rate was strongly dependent on the injector geometry, and increased noticeably with increasing the swirl intensity of the oxygen jet due to an increase of the oxygen flow velocity in the chamber and of the gas density near the fuel wall by swirling gas motion.

The applications of swirling mixers are not limited to aerospace fields, such as hybrid rocket engines, but it has potential application in non-aerospace fields that involve with mixing of two fluids, such as chemical engineering (oil and gas industry, chemical processing/production plants). Therefore, the approach outlined in this work has broad applicability.

1.3 Objectives of This Research

The main objectives of this research are:

i) Develop an analytic methodology for design of a counter-rotating vortex pair (CVP) mixer.

ii) Develop an experimental facility capable of characterizing the three-dimensional velocity field produced by CVP devices.

iii) Optimize the design of the CVP mixer by studying the effects of variations of design variables including swirl level, number of vanes, initial vane angle and other features.

Chapter 2 of this document describes the approach taken to satisfy the first two objectives. The chapter provides background on the theoretical methodology employed in generating CVP designs, and describes the experimental facility used to assess mixer performance. Chapter 3 provides information relative to the third and forth objective. This chapter contains a description of test articles developed using rapid prototyping infrastructure, and presents results of measured flow fields produced by these test articles. The thesis concludes with a summary in Chapter 4.

CHAPTER 2. MIXER DESIGN AND EXPERIMENT FACILITY

2.1 Mixer Design Approach

The proposed swirl mixer is designed to induce counter rotating vortices based on the potential flow theory. The design methodology presumes that the flow is incompressible and irrotational. Milne-Thomson's Circle Theorem[3] is applied to impose the constraint of the cylindrical tube enclosing the vortex pair. A Rankine vortex is utilized to eliminate the singularity that occurs at the center of the potential vortex. The superposition of counter-rotating potential vortices, combined with the constraint of flow tangency at the cylindrical boundary housing the vortices provides a methodology to completely describe the flow field on a potential basis.

2.1.1 Milne-Thomson's Circle Theorem

Figure 2.1 illustrates the overall geometry and coordinate system for the analytic approach. The circle theorem gives a complex potential for a fluid flow when a cylinder is placed into the flow. Let there be irrotational two-dimensional flow of incompressible inviscid fluid in the complex plane or z-plane and no rigid

boundaries. If a circular cylinder is introduced into the field of flow, the complex potential, F, becomes,

$$\mathrm{F} = \mathrm{f}(\mathrm{z}) + \bar{\mathrm{f}}\left(\frac{\mathrm{a}^2}{\mathrm{z}}\right) \tag{2.1}$$

where, $\mathrm{z} = \mathrm{x} + i\mathrm{y}$, *f*(z) is the complex potential of the flow and *a* is the radius of the cylinder. Based on the theorem, counter-rotating potential vortices of strength +/- Γ can be included at locations z_1 and z_2 to give:

$$F = \frac{i\Gamma}{2\pi}\log(\mathrm{z} - \mathrm{z}_1) - \frac{i\Gamma}{2\pi}\log(\mathrm{z} - \mathrm{z}_2) - \frac{i\Gamma}{2\pi}\log\left(\mathrm{z} - \frac{\mathrm{a}^2}{\overline{z_1}}\right) + \frac{i\Gamma}{2\pi}\log\left(z - \frac{a^2}{\overline{z_2}}\right) \tag{2.2}$$

where, $\overline{\mathrm{z}_1}$ and $\overline{\mathrm{z}_2}$ are conjugates of z_1 and z_2 respectively. Physically, the vortices at $\overline{\mathrm{z}_1}$ and $\overline{\mathrm{z}_2}$ represent images of the main vortices. These images lie outside the circle as illustrated in Figure. 2.1.

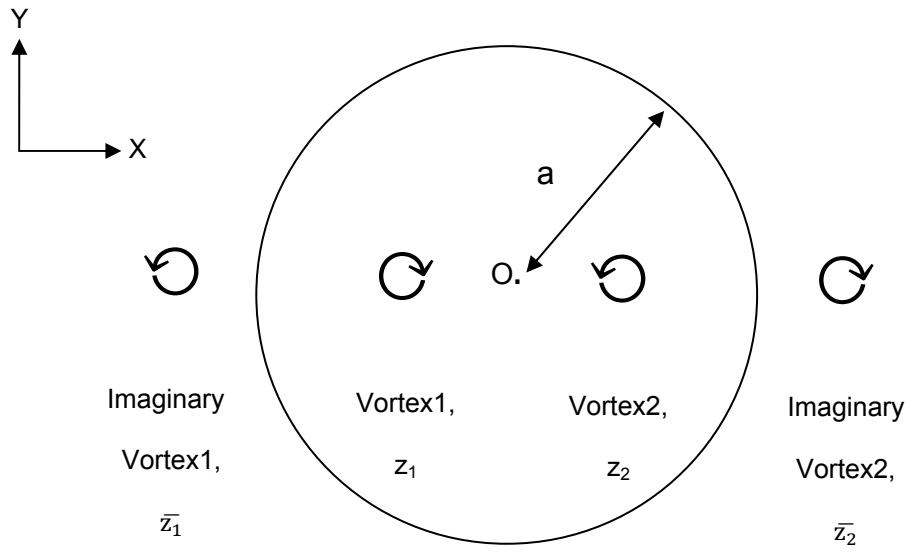

Figure 2.1 Vortex pair in cylinder

Complex velocity potential, W, is defined as $W = \frac{dF}{dz}$. Since F is supposed to be analytic, W will be a point function whose value is independent of the direction in which it is calculated. That is,

$$W = \frac{dF}{dz} = \frac{\partial F}{\partial x} = \frac{\partial \Phi}{\partial x} + i\frac{\partial \psi}{\partial x} = u - iv$$

$$= -\frac{i\Gamma}{2\pi}\frac{1}{z-z_1} + \frac{i\Gamma}{2\pi}\frac{1}{z-\frac{a^2}{\overline{z_1}}} + \frac{i\Gamma}{2\pi}\frac{1}{z-z_2} - \frac{i\Gamma}{2\pi}\frac{1}{z-\frac{a^2}{\overline{z_2}}} \quad (2.3)$$

In Cartesian coordinate system, the complex velocity potential becomes

$$W = -\frac{i\Gamma}{2\pi}\frac{1}{x+iy-(x_1+iy_1)} + \frac{i\Gamma}{2\pi}\frac{1}{x+iy-\frac{a^2}{x_1-iy_1}} + \frac{i\Gamma}{2\pi}\frac{1}{x+iy-(x_2+iy_2)} - \frac{i\Gamma}{2\pi}\frac{1}{x+iy-\frac{a^2}{x_2-iy_2}}$$

$$= -\frac{i\Gamma}{2\pi}\frac{(x-x_1)-i(y-y_1)}{(x-x_1)^2+(y-y_1)^2} + \frac{i\Gamma}{2\pi}\frac{(x_1^2+y_1^2)[x(x_1^2+y_1^2)-a^2x_1-iy(x_1^2+y_1^2)+a^2y_1]}{(x(x_1^2+y_1^2)-a^2x_1)^2+(y(x_1^2+y_1^2)+a^2y_1)^2} + \frac{i\Gamma}{2\pi}\frac{(x-x_2)-i(y-y_2)}{(x-x_2)^2+(y-y_{21})^2} -$$

$$\frac{i\Gamma}{2\pi}\frac{(x_2^2+y_2^2)[x(x_2^2+y_2^2)-a^2x_2-iy(x_2^2+y_2^2)+a^2y_2]}{(x(x_2^2+y_2^2)-a^2x_2)^2+(y(x_2^2+y_2^2)+a^2y_2)^2} \qquad (2.4)$$

Where z=x+iy. Therefore, the velocity components in Cartesian coordinate are defined by,

$$u = \frac{\partial\phi}{\partial x} = \frac{\Gamma}{2\pi}\left(\frac{-(y-y1)}{(x-x1)^2+(y-y1)^2} + \frac{y-y2}{(x-x2)^2+(y-y2)^2} + \frac{(x_1^2+y_1^2)[y(x_1^2+y_1^2)+a^2y_1]}{(x(x_1^2+y_1^2)-a^2x_1)^2+(y(x_1^2+y_1^2)+a^2y_1)^2}\right.$$

$$\left. - \frac{(x_2^2+y_2^2)[y(x_2^2+y_2^2)+a^2y_2]}{(x(x_2^2+y_2^2)-a^2x_2)^2+(y(x_2^2+y_2^2)+a^2y_2)^2}\right)$$

$$= \frac{\Gamma}{2\pi}\left(\frac{-(y-y1)}{(x-x1)^2+(y-y1)^2} + \frac{y-y2}{(x-x2)^2+(y-y2)^2} + \frac{y(x_1^2+y_1^2)+a^2y_1}{x^2(x_1^2+y_1^2)-2a^2xx_1+a^4+y^2(x_1^2+y_1^2)+2a^2yy_1}\right.$$

$$\left. - \frac{y(x_2^2+y_2^2)+a^2y_2}{x^2(x_2^2+y_2^2)-2a^2xx_2+a^4+y^2(x_2^2+y_2^2)+2a^2yy_2+a^4}\right)$$

$$= \frac{\Gamma}{2\pi}\left(\frac{-(y-y_1)}{(x-x_1)^2+(y-y_1)^2} + \frac{y-y_2}{(x-x_2)^2+(y-y_2)^2} + \frac{y(x_1^2+y_1^2)+a^2y_1}{(xx_1-yy_1-a^2)^2+(xy_1+x_1y)^2} - \frac{y(x_2^2+y_2^2)+a^2y_2}{(xx_2-yy_2-a^2)^2+(xy_2+x_2y)^2}\right)$$

(2.5)

$$v = \frac{\partial\phi}{\partial y} =$$

$$\frac{\Gamma}{2\pi}\left(\frac{x-x_1}{(x-x_1)^2+(y-y_1)^2} - \frac{x-x_2}{(x-x_2)^2+(y-y_2)^2} + \frac{x(x_1^2+y_1^2)-a^2x_1}{(xx1-yy_1-a^2)^2+(x_1y+xy_1)^2} - \frac{x(x_2^2+y_2^2)-a^2x_2}{(xx_2-yy_2-a^2)^2+(x_2y+xy_2)^2}\right)$$

(2.6)

2.1.2 Rankine Vortex

A Rankine vortex is used to avoid unbounded velocities that are created near the centers of the potential vortices. A Rankine vortex utilizes a solid body rotation in the core, surrounded by a free (i.e. potential) vortex. The tangential velocity of the Rankine vortex is defined in terms of the radial distance from the vortex center, r, as shown in Figure. 2.2:

$$v_\theta = \frac{\Gamma r}{2\pi R_R^2} \; (r > R_R) \qquad (2.7)$$

$$= \frac{\Gamma}{2\pi r} \; (r > R_R)$$

Where R_R is a Rankine vortex radius, i.e. the point where flow transitions from solid body rotation to potential vortex rotation. In Cartesian coordinates, r can be expressed:

$$r = \sqrt{(x - x_0)^2 + (y - y_0)^2} \qquad (2.8)$$

and the velocity components are:

$$u = -v_\theta \sin\theta, \; v = v_\theta \cos\theta \qquad (2.9)$$

where, θ is the angle between x-direction and y-direction vectors at the grid points, and obtained by,

$$\theta = \tan^{-1}\frac{y-y_0}{x-x_0} \tag{2.10}$$

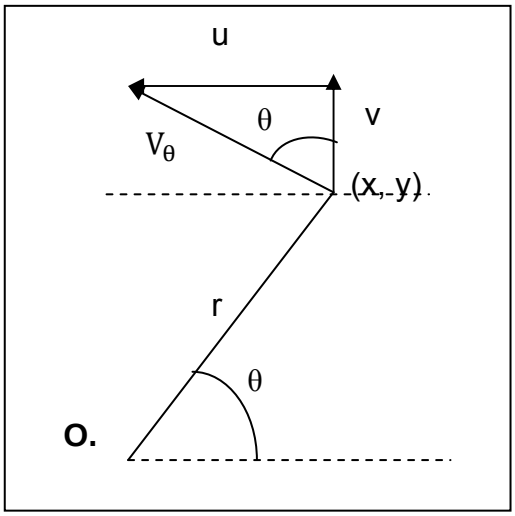

Figure 2.2 Velocity vector description (Point O is at a vortex center)

2.1.3 Flow Turning Angle Calculation

Physically, the amount of swirl imparted to the flow is controlled by the vortex strength, Γ . The local swirl angle imposed by vanes that are aligned with the flow can be determined by superposing a uniform axial flow of magnitude w to the cross-stream velocity components in Eq. 2.9. Let α be the local vane angle with respect to the axial direction and α_{max} be the maximum swirl angle prescribed at location at r = R_R. With a fixed axial velocity, w, fluid velocity through the swirl injector, v_α, becomes

$$v_\alpha = w \times \tan \alpha_{max} \tag{2.11}$$

Substitution of equation (2.11) into equation (2.7) gives the vortex strength in terms of w and α_{max} as shown in equation (2.12).

$$\Gamma_{max} = 2\pi R_R \times w \times \tan \alpha_{max} \tag{2.12}$$

Assuming vortex strength varies linearly along the axial direction, we can write:

$$\Gamma = \Gamma_{max} \times \left(\frac{z}{L}\right) = 2\pi R_R \times w \tan \alpha_{max} \times \left(\frac{z}{L}\right) \tag{2.13}$$

Where, z is axial distance and L is total axial length of the swirler. Here we should note that a flow that has axial variation in circulation does generate vorticity and for this reason, the potential flow treatment is not mathematically sound. However, the methodology employed here does provide a mathematical basis to define vane shapes and the predicted flowfields do match measured flowfields as discussed in the following chapter. However, many of the best performing designs did maintain a constant circulation along vane length and do in fact adhere to criteria required to guarantee and irrotational flow.

Combining equation (2.11) to (2.13), the local flow turning angle can be expressed:

$$\alpha = \tan^{-1}\left(\frac{v_\alpha}{w}\right) = \tan^{-1}[\tan \alpha_{max}\left(\frac{z}{L}\right)\left(\frac{r}{R_R}\right)] \qquad (r \le R_R) \tag{2.14}$$

$$= \tan^{-1}[\tan \alpha_{max}\left(\frac{z}{L}\right)\left(\frac{R_R}{r}\right)] \quad (r > R_R)$$

Figure 2.3 shows vane angle variation along a horizontal line passing through both vortex centers for a case where the maximum flow angle is +/- 45 degrees.

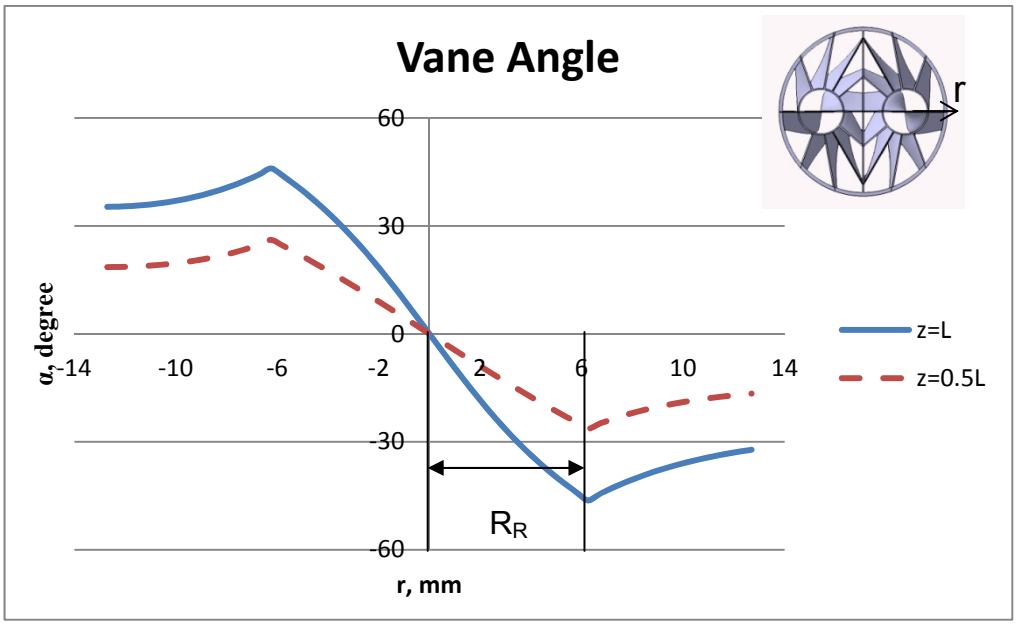

Figure 2.3 Flow turning angles at z = L and z = 0.5L (α_{max}= 45 degree)

2.2 Design Process

The theoretical approach described in the prior section provides a methodology to compute velocity vector components information over the entire flow field. Therefore, the velocity data facilitates to compute streamlines from any given grid points with desired angles of the flow. Streamlines are a family of curves that are instantaneously tangent to the velocity vector of the flow. These show the direction a fluid element will travel in at any point in time.

Streamlines are defined by

$$\frac{dx}{u} = \frac{dy}{v} = \frac{dz}{w} = ds \qquad (2.15)$$

Streamlines are obtained by solving the algebraic equations (2.5) and (2.6) at a given x,y,z location in the flow. Tecplot[4] provides a capability to generate these streamlines from the given velocity components and was therefore used to create the vane shapes from these data. To visualize streamlines from the velocity data, it uses a predictor-corrector integration scheme. The basic idea is to create the streamlines by moving a series of small steps from a starting point in the direction of, or in opposition to, the local vector field[5]. To design vanes, a series of starting points are chosen along the line of the vane leading edges. The integration is controlled by modifying step size, max steps, and minimum step size.

The generated streamlines can be extracted and written in form of ASCII file as a point format. The extracted points of the streamlines are then imported into a 3-D CAD software, CATiA[6] in order to construct the surfaces and solid bodies as shown in Figure. 2.4a below. The *Spline* function in CATiA facilitates creation of the curved vane coordinates in 3-D space using the imported points. Then, the vane coordinates are constructed into surfaces using the *Multi-Section Surface* function in CATiA. If the curved-vane surfaces have too much twist, they can create non-physical geometries that are evidenced by a failure of this function

due to the tangency constraints. The internal topological operator cannot correctly smooth the created multi-sections surfaces in this case. The *Thick Surface* function gives the thickness of the surfaces. Figure 2.4b shows the result of this process for a single vortex. Finally, for a pair of counter-rotating vortices, the design in Figure. 2.4c is generated. The design in Figure. 2.4c incorporates two vanes within the Rankine vortex portion of the vane with a ring support. Other alternatives were also investigated as described in Chapter 3.

a) 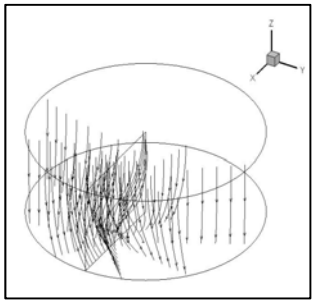 b) 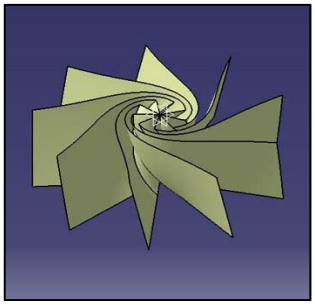 c) 

Figure 2.4 Design process a) Streamlines, b) Surfaces, c) Solid bodies

Figure 2.5 shows velocity vector contours obtained from the analytic analysis of a CVP mixer. The internal diameter of the mixer 50.8 mm (2 inches) in order to fit within existing hybrid rocket test hardware at the Maurice Zucrow Laboratory (MLZ). Each vortex center was located at the half radius 12.7 mm from the center of the circle on the X axis. The characteristic radius of the Rankine vortex, R_R, was chosen to be 6 mm. If R_R is too small, curved-vane surfaces have too much twist near the vortex centers and result in failure of surface extrusion due to the tangency constraints. If R_R is too large, the device essentially becomes a solid

body rotation swirler. The normalized axial velocity was uniform across the flow field with a magnitude of 1.

As with the classical vortex pair, a strong downflow is created in the region between the two vortices. In an unconstrained environment, this induced velocity will cause the pair of vortices to move downward as they convect downstream.

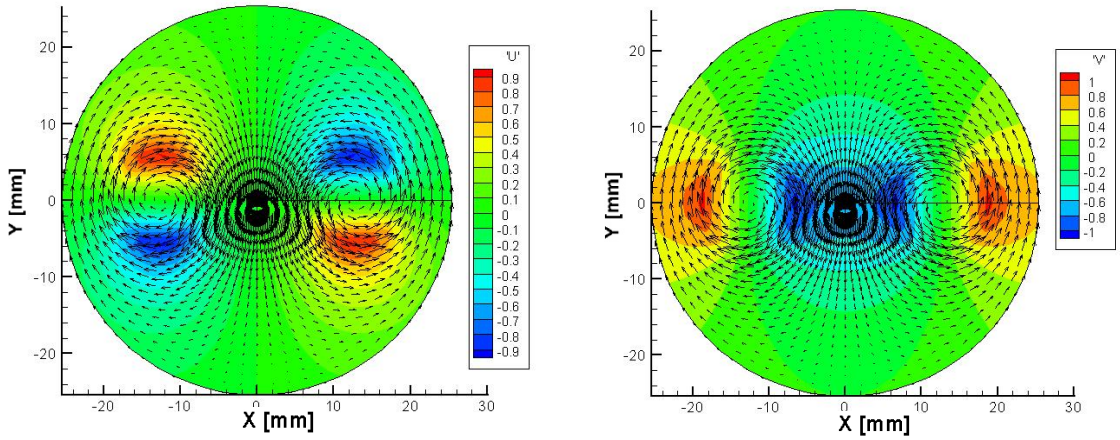

a) Ideal X-direction velocity, U b) Ideal Y-direction velocity, V

Figure 2.5 Ideal transverse velocity vector contours in a) X-direction and b) Y-directions respectively

2.3 Experimental Facility

An experimental facility was developed to measure the performance of CVP mixers. Local static and stagnation pressure measurements were used to compute local stream velocity and a mass flow rate under steady flow conditions. A seven-hole pressure probe was used to map the velocity vector fields for each test model. The measured data were normalized by the upstream velocity and

compared across different test models to assess the overall performance of a given swirler design configuration.

Test models were printed by Objet Eden350V 3D printer. Figure 2.6 provides images of a typical test article printed by the 3D printer. The printer is based on Objet's PolyJet photopolymer jetting technology that builds horizontal layers of 16-microns (0.0006 in) of model resin and support material. The print system is designed to provide high-quality, 3-dimensional models directly from a CAD STL file.

a)  b) 

Figure 2.6 Model-1 a) Front view, b) Rear view. The outer diameter of this part is 55.88 mm (2.2 inches)

2.3.1 Experiment and Measurement Setup

The experimental apparatus was installed in the Aerospace Science Laboratory (ASL) is located at the Purdue Airport. A commercial leaf blower was used as a simple way to facilitate variable airflows at velocities as high as 10 m/s. The working fluid for the tests is air and it is delivered from a commercial leaf blower.

The blower facilitates an easy control of the amount of air blowing with a rheostat (Figure 2.7). For the highly three-dimensional flow created from a CVP mixer, a seven-hole probe is employed for flow diagnostics. It provides information of velocity magnitude, velocity vectors, the local total and static pressures with flow inclined by 70° -75° with respect to the probe axis[7]. Positioning and movement of the 7-hole probe is controlled by a two-axis traverse system which is driven by dual stepper motors. Set-up of the traverse system is shown in Figure 2.8. The vertical slider is bolted onto the traverse platform of the horizontal slider for 2-axis movement and the 7-hole probe is aligned with respect to the axes.

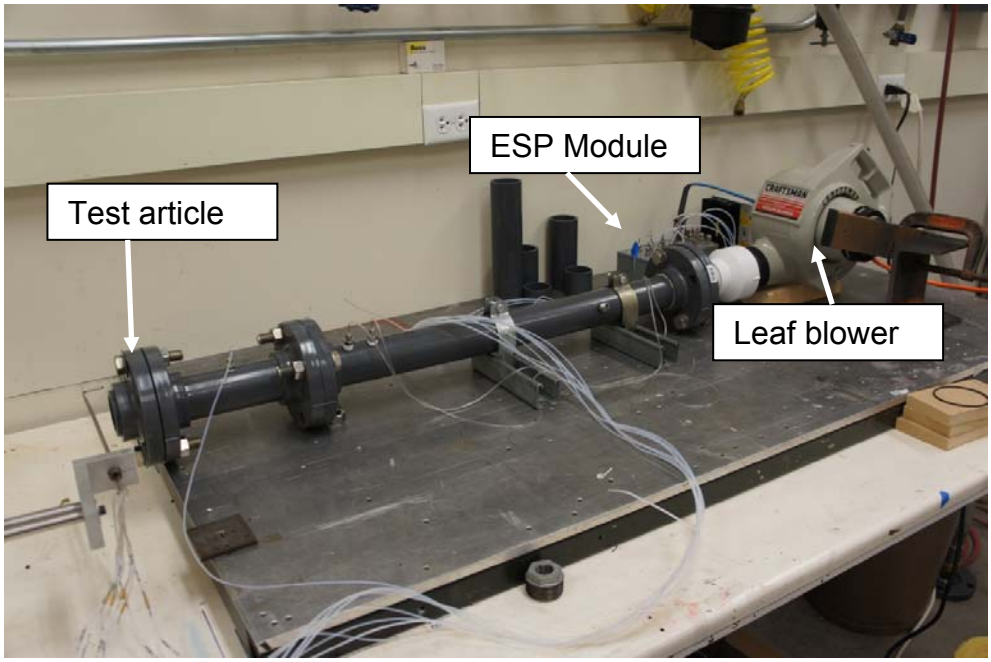

Figure 2.7 Air supply system by an electric wind blower

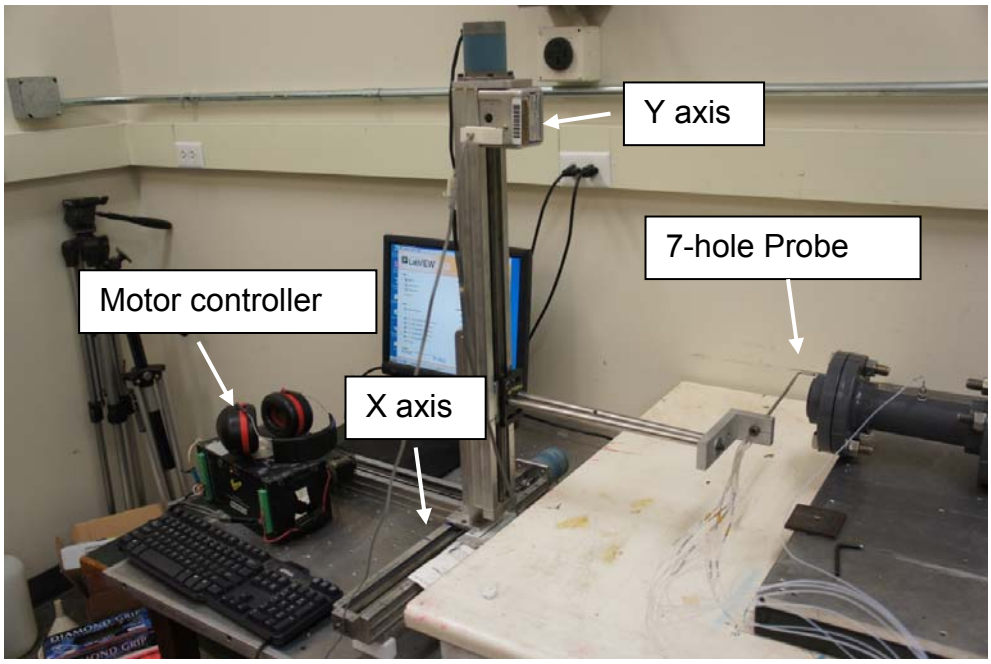

Figure 2.8 Electric traverse system

The motors are controlled by Velmex NF90 controller. The Nf90 is a programmable stepping motor controller for running up to three motors, one-at-a-time. The NF90 has capabilities of 400 steps per revolution (0.9° step angle) resolution and incremental index distance is programmable from ±1 to ±1,048,575 steps. Acceleration/Deceleration is settable from 2,000 to100,000 steps/sec^2 in 2,000 step/sec^2 increments and speed is programmable from 1 to 6000 steps/sec in 1 step/sec increments.

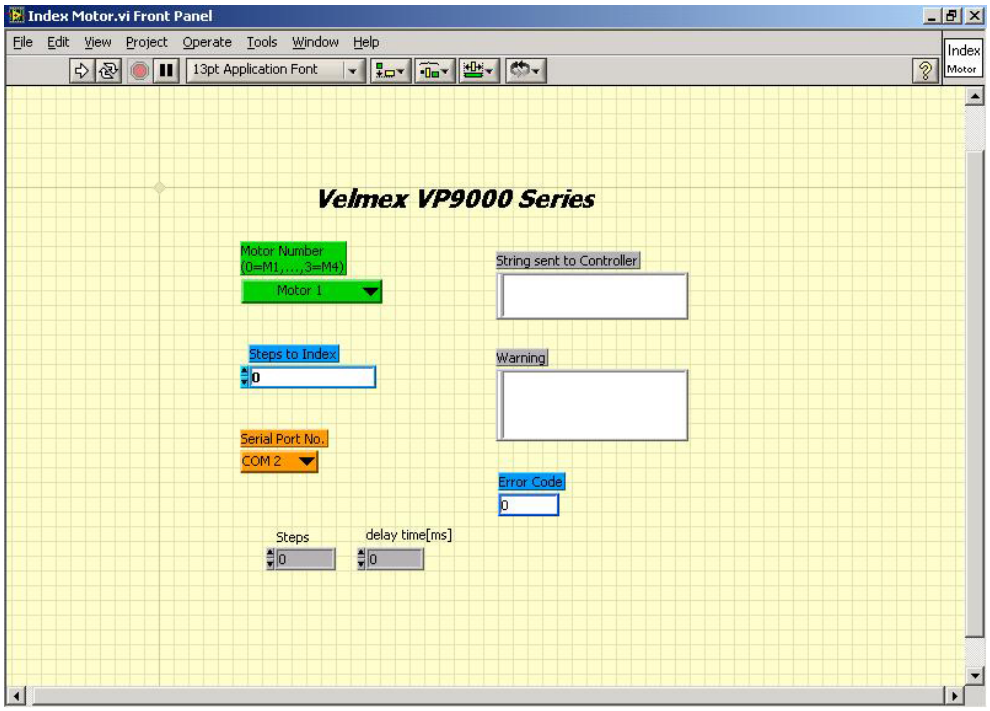

Figure 2.9 Front panel of LabView VI for the motor controller

The LabVIEW VI (Virtual Instrument) for the VELMEX NF90 can be seen in Figure 2.9. The VI is programmed to send commands to the motor controller and controls the traverse system. It is capable of choosing the motors and controlling steps and delay-time between the steps. This Labview code also shows warning messages and error codes when the commands are inappropriate.

The cylindrical flow path is made of a 2” schedule 80 PVC pipe, which has 1.915” of internal diameter and 3.35’ of the total length. Figure 2.10 shows a schematic drawing of the experimental apparatus developed for the research. Stagnation and static pressures are measured upstream of the mixer in order to calculate mass flow rates. The velocities of the incoming flows are computed based on the

difference between the stagnation and static pressures, and thereby obtaining the mass flow rate with an assumption that air flow is steady and incompressible. The velocity of the uniform flow is also used to non-dimensionalize the seven-hole probe data. This provides a benefit of comparing results when the uniform velocities are different from one another.

An electronically-scanned pressure measurement module (ESP), which is a gauge pressure transducer, is used for data acquisition from the seven-hole probe and the pressure taps. The output signals from the ESP module are digitized and recorded using a National Instruments data acquisition system, Labview as discussed in detail in Section 2.3.3. Temperature is not a factor in the seven-hole probe pressure readings as pressures are obtained by non-dimensional coefficients based on readings of all seven port measurements[8]. The air flows through a screen upstream of the test article in order to remove any velocity profiles induced by the flow through the plumbing system.

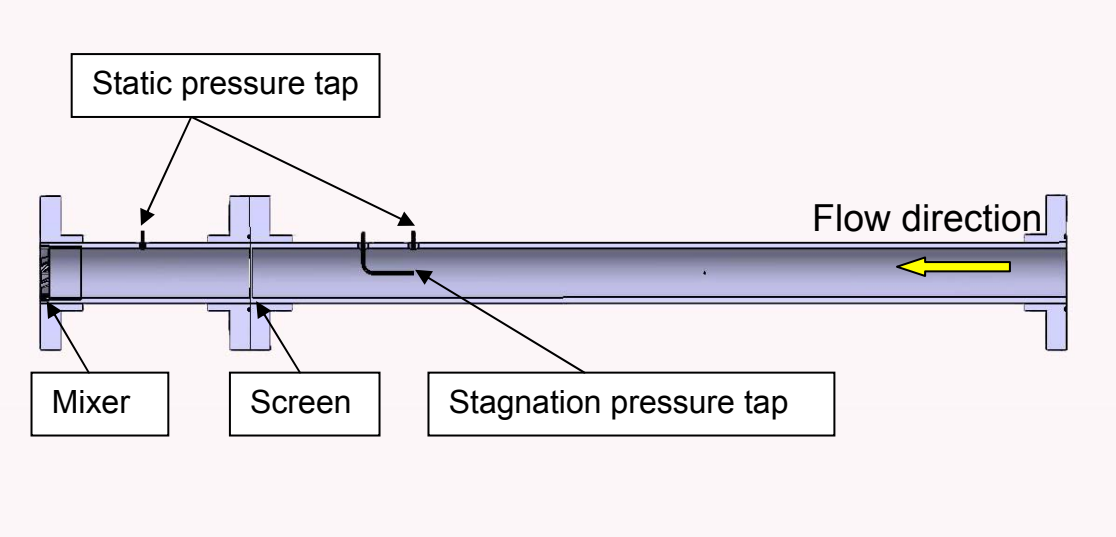

Figure 2.10 Schematic drawing of the experimental apparatus

Each of the exit tubes in the 7-hole probe has an outer diameter of 0.040” and the ESP module has 0.063” of taps which are connected to the transducers. Tygon R3603 flexible tubing was used and TC 063-040R stainless steel tubing reducers are needed to adapt 0.063" tubing down to 0.040" tubing for the connection between the seven-hole probe and the ESP module. Communication with the ESP module is achieved via the Ethernet interface cable using industry standard TCP/UDP/IP protocols. This ESP module holds an accuracy of ±0.04% over its range of 15 psid.

2.3.2 Seven-Hole Pressure Probe

For the highly three-dimensional flow from a CVP mixer, a seven-hole probe is employed for flow diagnostics. It provides information of velocity magnitude, velocity vectors, the local total and static pressures with flow inclined by 70° -75°

with respect to the probe axis[7]. A seven-hole probe is constructed by surrounding a central pressure port with six equally spaced ports as illustrated in Figure. 2.11 below. The port reading the highest pressure is indicative of the general direction of the flow. If the center port reads the highest pressure, the flow is considered to be a low angle flow (below 20^0) and the data from all seven pressure ports is used in data reduction. If, however, a peripheral port reads the highest pressure, then the flow is considered to be a high angle flow, and there is a significant possibility of flow separation over the ports. The pressure information that is provided by any holes in the separated region is not useful in the calculation. In a high angle flow, the flow is therefore calculated based only on the port with highest pressure and the three adjacent ports, where the flow is known to be attached[7].

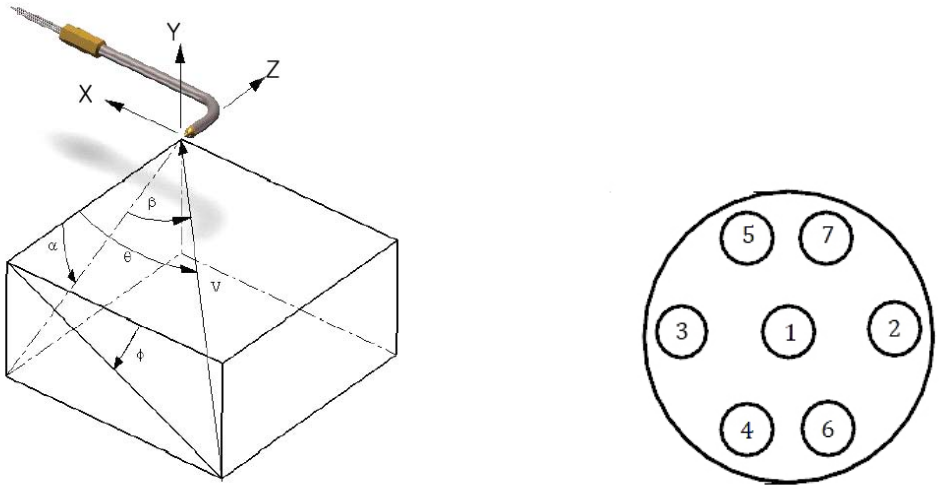

Figure 2.11 Seven-hole probe coordinate and port locations

The probe tip could be either hemispherical or conical in shape, depending on the application and requirement of the study. In general, a blunt tip provides a greater range on flow range, but sensitivity would be compromised[8].

Seven-hole probes are made very small to minimize disturbance to the flow. However, they are very sensitive to manufacturing defects. As a result, each probe must be individually calibrated prior to use. Calibration defines a relationship between the port pressure readings and the actual velocity of the fluid flow. Typically, the calibration process consists of placing the probe in a uniform flow of known velocity, direction, density, temperature, and static pressure[8]. The probe is then rotated and pitched through a range of known angles maintaining the probe tip location fixed in order to simulate every possible measurable velocity directions. Because calibration of a 7-hole probe is based solely on probe geometry, it keeps its characteristics and only one calibration is required for the lifetime of the probe unless the probe is physically damaged.

According to the manufacturer, the static accuracy of the pressure transducers used for probe calibration is 0.1% of full-scale reading. In order to minimize the effect of ambient air temperature changes during calibration, the transducers periodically undergo an automated zero-offset calibration process. The cone and roll positioning have resolutions of 0.9 degrees and are both equipped with rotational encoders, providing an accuracy of 0.01 degrees[8]. The probes are calibrated with a specific coordinate system fixed at the tip of the probe, and the

probe must be mounted in the test section in the same orientation[7]. The probe should be aligned so that ports one, two and three are aligned horizontally (or along the X axis in Figure 2.11). These ports are used to measure the yaw angle (β). Ports one, four, five, six and seven should be aligned vertically (or along the Y axis in Figure 2.11). These ports are used to measure the pitch angle (α).

The probe should not be placed closer than 4-5 tip diameters to another body due to the manner that it was calibrated[7]. Therefore, data measured too close to a solid wall or test article, such as boundary layer measurements, are normally not reliable.

For this research, an “L”-shaped 7-hole probe with a conical shape tip purchased from The Aeroprobe Corporation is used. The specification of the probe, model C06-58-1, consists of the tip diameter of 0.125" (3.18mm) and the ports diameter of 0.020" (0.508mm). The materials used for fabrication are a combination of brass and stainless steel.

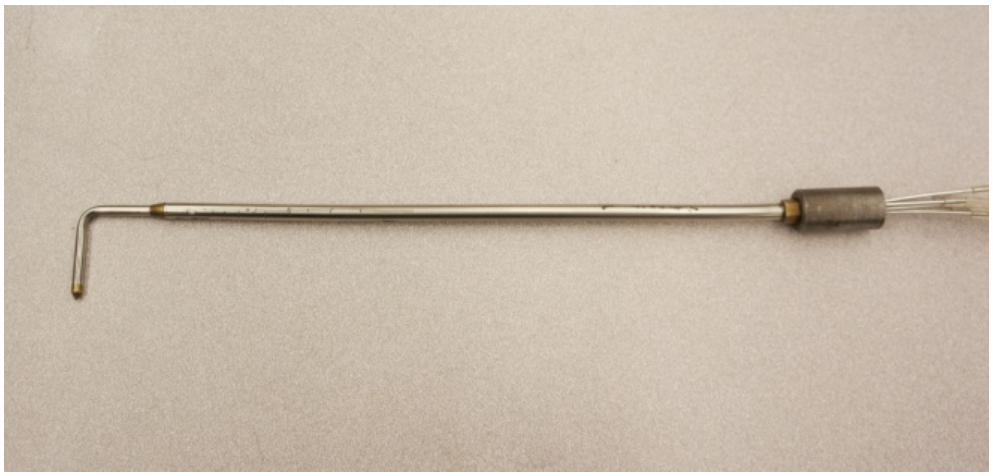

Figure 2.12 “L”-shaped 7-hole probe with a conical shape tip

Data reduction is performed using the Multiprobe software, which is a pressure-to-velocity reduction software provided by the manufacturer. It is a program used to post-process data taken with the seven-hole probes, and it computes meaningful aerodynamic quantities such as angles, velocity, Mach number, and characteristic pressures by using the probe’s calibration map and pressure data acquired from a probe. It utilizes a local-least squares (LLS) fit of the pressure acquired to the closest calibration points. The LLS searching algorithm uses specialized multi-region search routines and angular range validation routines to improve accuracy[8].

The uncertainty in the measurement of velocity in an unknown flow field (the end goal of this analysis) is dependent on the errors accumulated during the probe calibration process and also the errors associated with the actual measurement using the calibrated probe. Figures 2.13-2.15 illustrate average errors that probe

will produce from the data reduction if it is used outside of the calibration range. The M### notation indicates a pre-processed calibration file for the seven-hole For example, M101 corresponds to a Mach number of 0.101 with analogous designations for the other Mach numbers shown in the plot. At the lowest speed (M101) calibration curve most applicable to the measurements taken, the seven-hole probe provides excellent accuracy over a range of flow speeds/Mach numbers.

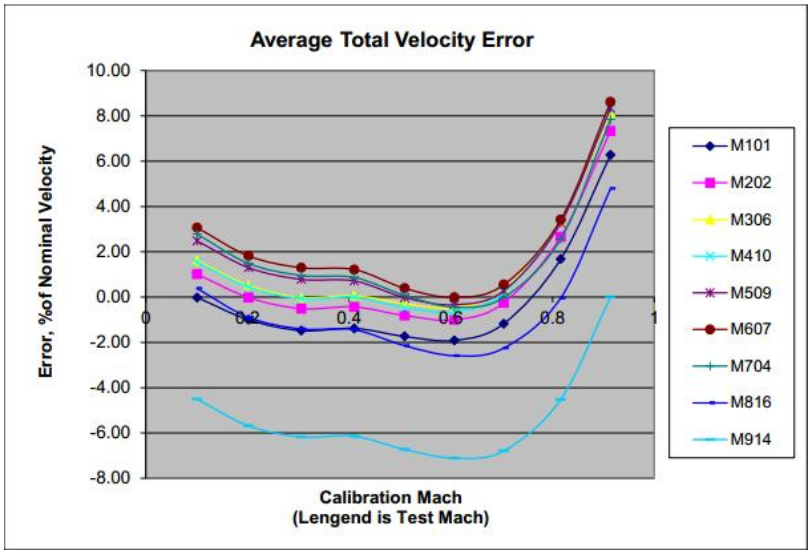

Figure 2.13 Average total velocity error

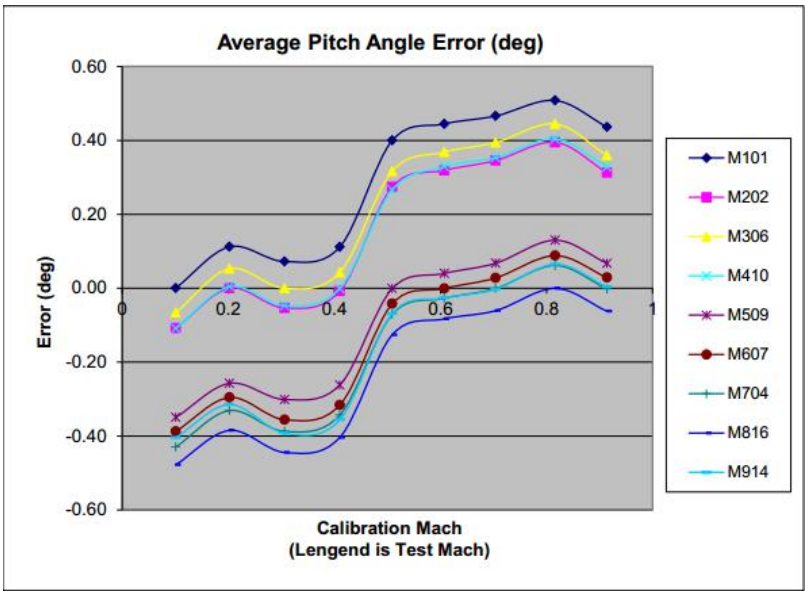

Figure 2.14 Average Pitch angle error

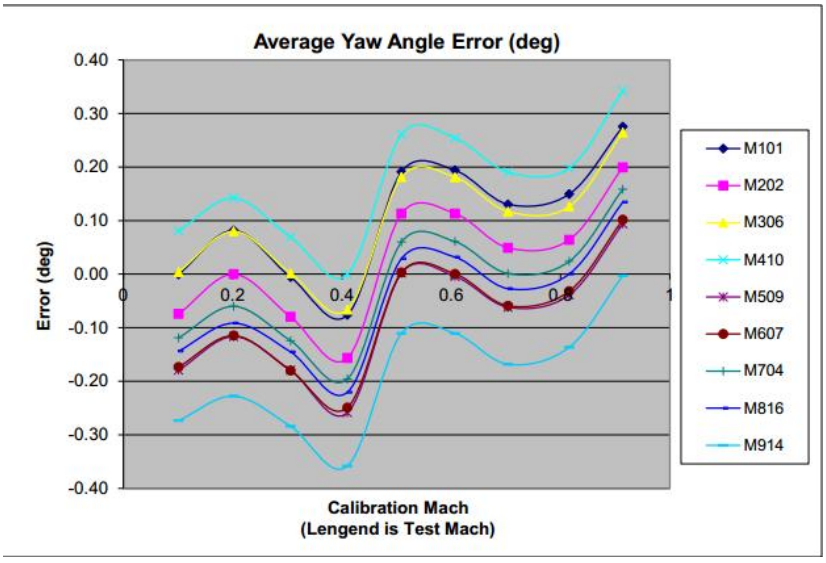

Figure 2.15 Average yaw angle error

2.3.3 Electronically Scanned Pressure Measurement (ESP) Module

The model 9116 Pneumatic Intelligent Pressure Scanner is used to scan pressure data from the 7-hole probe. It is a high performance pressure acquisition module for multiple measurements of dry, non-corrosive gases having 16 integral pressure transducers. This ESP module provides up to ±0.05% FS(Full Scale) system accuracy[19]. The output signals from the sensors are digitized and recorded using a National Instruments data acquisition system, Labview. A network switch facilitates the connection of multiple ESP modules to a host computer; otherwise, network crossover cables are required.

Figure 2.16 Model 9116 Intelligent Scanner (ESP module)

2.3.4 Labview VI

The LabVIEW VI created specifically for the ESP module can be seen in Figure 2.17. The VI allows the user to conveniently connect the module to the host computer and run the data acquisition system. It is capable of controlling data acquisition frequency and re-zeroing the 16 pressure transducers of the ESP module. This Labview code also displays the sensor output on the screen and record it to excel spreadsheets for post processing.

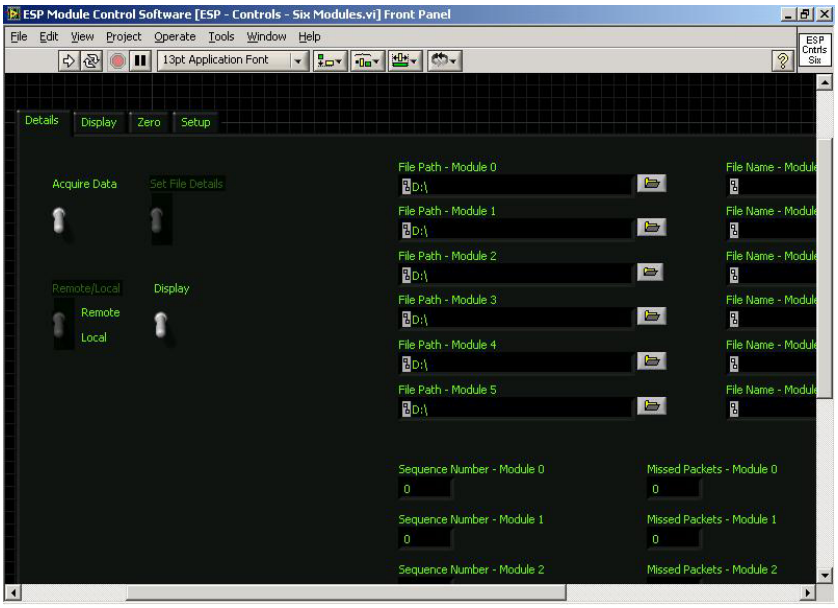

Figure 2.17 Front Panel of LabVIEW VI for the ESP module

2.4 Application in Hybrid Rocket Engine

At present, nearly all components in aerospace rely on classical manufacturing processes. With respect to mixers or injectors, they deliver fluids through cylindrical holes/orifices that are typically formed via drilling or laser or electric

discharge machining. However, the advent of direct metal laser sintering (DMLS) technologies foster new and more cost-effective capabilities and provide an alternative for development of unique injector concepts than those currently employed in cylindrical hole or etched channel devices.

The Direct Metal Laser Sintering (DMLS) technologies directly produce metal parts on the basis of three-dimensional CAD data in STL file format. It builds up layers by melting metal powder with a laser beam and enables to create parts including extremely complex geometries. In order to avoid metal oxidation during the process, the system operates in both protective nitrogen and argon atmospheres, thereby facilitating to process a wide range of materials. Currently available materials for the manufacturing are stainless steel, aluminum, titanium, and even high nickel steels (Inconnel). This capability provides the path toward fabrication of complex injector design concepts even for arduous combustor environments. Therefore, DMSL products have high detail resolution and surface quality with desired mechanical properties.

a)  b) 

Figure 2.18 A CVP mixer (Model 10) manufactured by DMLS technology.

Figure 2.18 provides images of a 2 inch (50.8 mm) diameter CVP fabricated from Inco 718 using the DMLS process. The mixer was built up with 20 micron layers, and it allowed having 0.4 mm thickness vanes without structural defects. Static pressure drops due to the mixer configurations were measured in a hybrid rocket test rig at MLZ.

CHAPTER 3. RESULTS

Using the design methodology described in Chapter 2, a variety of CVP mixers were fabricated using the Objet PolyJet photopolymer printer; a typical example was shown in Fig. 2.6. Section 3.1 provides a summary of the design characteristics of all the models fabricated in this fashion, including DMLS-manufactured parts described below.

The swirling flow produced by the mixers was then assessed via a x-y traverse of the flow exiting the mixer. The x-y traverse was performed a distance of 1.25 cm (0.5 inches) downstream of the exit as a compromise to mitigate potential interference with the $1/8^{th}$ inch probe. Velocity data were normalized by the velocity entering the mixer in order to compensate for slight test-to-test variation of the incoming flow velocity. Flow fields were surveyed using a 20 by 20 mesh with a 0.125” step size and contours of X, Y, and Z velocity (u, v, w) were plotted using consistent legends in order to easily compare results from mixer to mixer. The velocity field maps were used to validate the design approach and to evaluate the ability of a given design to approach the theoretical velocity distribution obtained using the analytic model. The theoretical results neglect the

vane thickness whereas finite vane thickness creates a blockage of cross-sectional flow area and trailing wakes behind each of the vanes. Section 3.2 provides a summary of these investigations.

A preferred configuration was selected based on these evaluations, and several metal CVP mixers were fabricated from Inco718 using direct metal laser sintering as discussed in Chapter 2. These articles were inserted in a hybrid rocket test rig for evaluation of pressure drop characteristics. Gross mixing performance under hotfire conditions will be reported in the near future by Steven Shark[21].

3.1 Summary of Model Designs

Figure 3.1 highlights design variables investigated during the study. The size of the ring support which structurally supports vanes at the transition of solid body rotation and the potential flow vortices, R_s was investigated. The initial and final/maximum vane angles (α_i , α_{max}) at the location $r = R_R$ were also studied as was the overall thickness of the mixer, L. Finally, the number of vanes in both solid body rotation and potential vortex rotation sections were varied.

Manufacturing and material strength limitations ultimately set the vane thickness that can be employed. After many tries, vanes with 0.7 mm thickness were determined to be the thinnest that can be printed using the Objet PolyJet printer without having a deformation. This thickness also limited the number of potential vortex vanes given overall solidity considerations. For the DMLS-manufactured

parts, we experimented with this thickness as well and found that excellent quality was obtained using a vane thickness of 0.4 mm (400 microns).

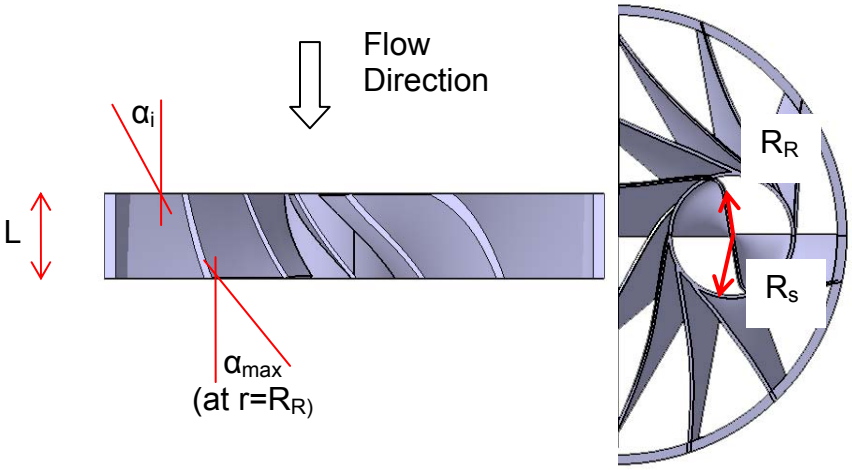

Figure 3.1 Design variables

Table 3.1 summarizes the designs of fifteen models successfully fabricated and evaluated using 7-hole probe surveys or hybrid rocket test article evaluation. Most of the designs incorporated a maximum vane angle of 45 degrees and a swirler thickness of 8.5 mm (1/3 inch). A detailed discussion of flowfield maps from each of the mixers is provided in the following section.

Table 3.1 Test matrix

M-#	α_{max} [deg]	α_i [deg]	R_R [mm]	R_S [mm]	L [mm]	# of Vanes		Test Vel. [m/s]	Vane Angular Locations ($r>R_s$)
						$r>R_s$	$r<R_s$		
1	45	0	6	6.6	8.5	10	6	5.4	0,60,90,120,150,180 ,210,240, 270 & 300
2	45	0	6	6.6	16.9	10	6	5.4	Same as Model #1
3	45	45	6	6.6	8.5	10	6	5.1	Same as Model #1
4	45	45	6	6.6	8.5	10	2	5.3	Same as Model #1
5	45	45	6	7.6	8.5	10	2	5.4	Same as Model #1
6	45	45	6	6.6	8.5	10	2	5.3	0,60,90,110,130,170 ,210,240,270 & 300
7	45	45	6	3.6	8.5	10	0	5.2	Same as Model #6
8	45	45	6	6.6	8.5	10	0	5.4	0,70,100,120,140,18 0,210,240,270 &300
9	45	45	6	6.6	8.5	10	2	5.2	Same as Model #8
10	45	45	6	6.6	8.5	10	2	5.7	0,70,100,120,140,18 0,220,240,260& 290
11	45	45	6	6.6	8.5	11	2	5.3	0,70,100,120,140, 180,220,230,250, 260 & 290
12	30	30	6	6.6	8.5	10	2	5.8	Same as Model #10
13 (DMLS)	45	45	6	6.6	8.5	10	2	-	Same as Model #10 Vane Thickness = 0.4mm
14 (DMLS)	15	15	6	6.6	8.5	10	2	-	Same as Model #10 Vane Thickness = 0.4mm

3.2 Experiment results

Models were designed based on data from the analytical approach discussed in Chapter 2 and the influence of all major design variables was considered as highlighted in Table 3.1. The performance of a given design was primarily assessed from a velocity field survey near the exit of the mixer as discussed in Chapter 2. For promising designs, surveys were also taken at distances further downstream for both internal and external flow from the mixer. These results are highlighted in the following sections of this chapter.

3.2.1 Model #1 (M-1)

Model M-1 was the first design successfully fabricated using the Objet Polyjet printer. This model incorporated twisted vanes that varied in angle from $\alpha_i=0$ to a maximum downstream angle (α_{max}) of 45 degrees at $r=R_R$. The model incorporated 6 vanes in the solid body region of the Rankine vortex and 10 vanes in the potential flow region. Vane angles and other dimensions are noted in Table 3.1.

Figure 3.2 highlights the design and the velocity profiles near the exit plane of the swirler. The results clearly show the existence of the counter rotating vortices with topology analogous to the analytic prediction shown in Figure. 2.5. The device produces a very uniform axial flow and this was viewed to be a desirable characteristic in evaluating designs, i.e. If the axial flow has large variations, this implies variation in flow resistance at various locations in the exit plane.

However, the M-1 transverse velocities were significantly lower than those predicted by theory as the vane pattern did not impart as much swirl as desired. For this reason, the M-1 design was less than optimal.

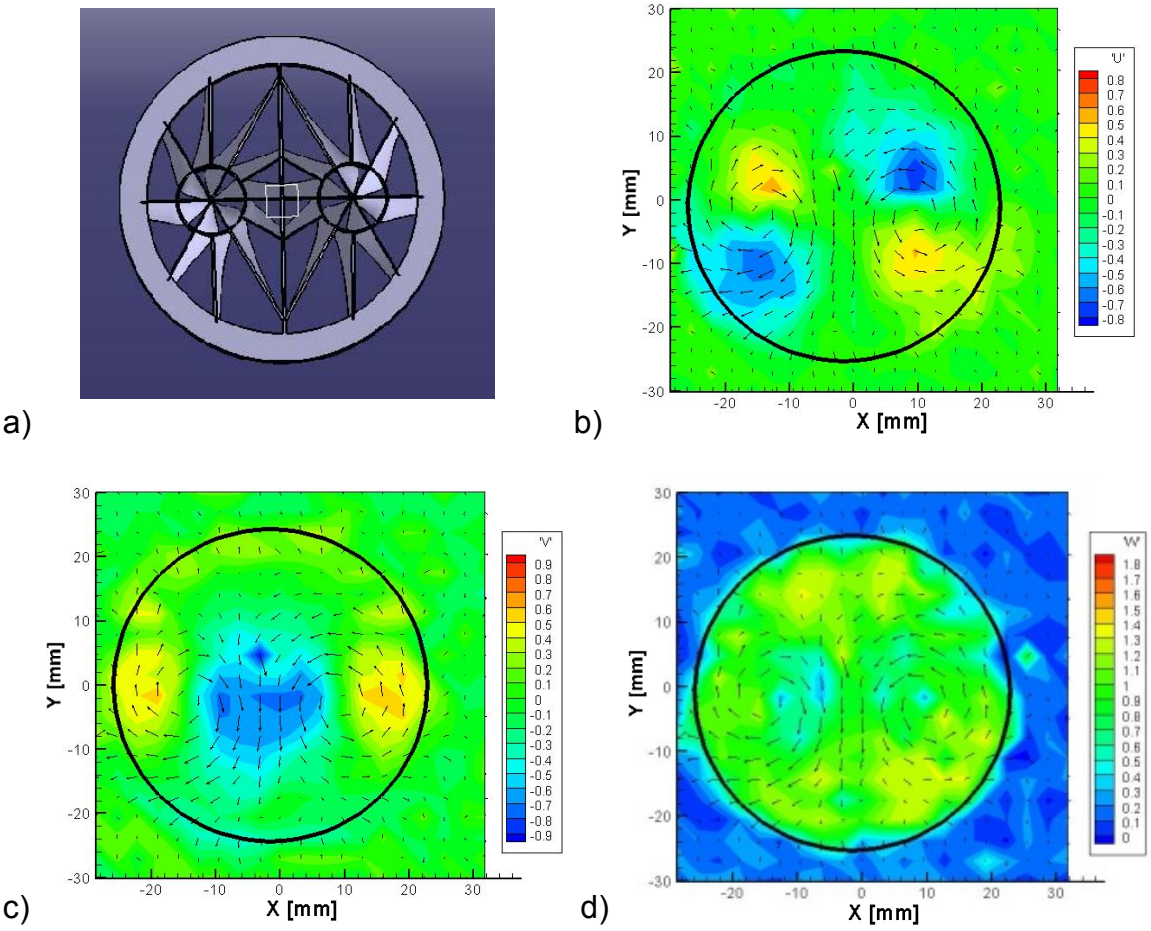

Figure 3.2 Contour of velocity vector fields for Models 1 a) Axial view from inlet side, b) lateral velocity, u, c) vertical velocity, v, d) axial velocity, w

3.2.2 Model #2 (M-2)

M-2 is designed to assess the effect of the axial length, L and is otherwise identical to M-1. The length/thickness of the swirler was doubled in this case to assess effects of this variable. As noted in Figure. 3.3, the design produced swirl levels comparable to M-1 and improved axial flow uniformity somewhat. In

general, the flow field was quite similar to the thinner M-1 design. For this reason, the swirler length (L) of 8.5 mm (1/3”) was used on all subsequent designs.

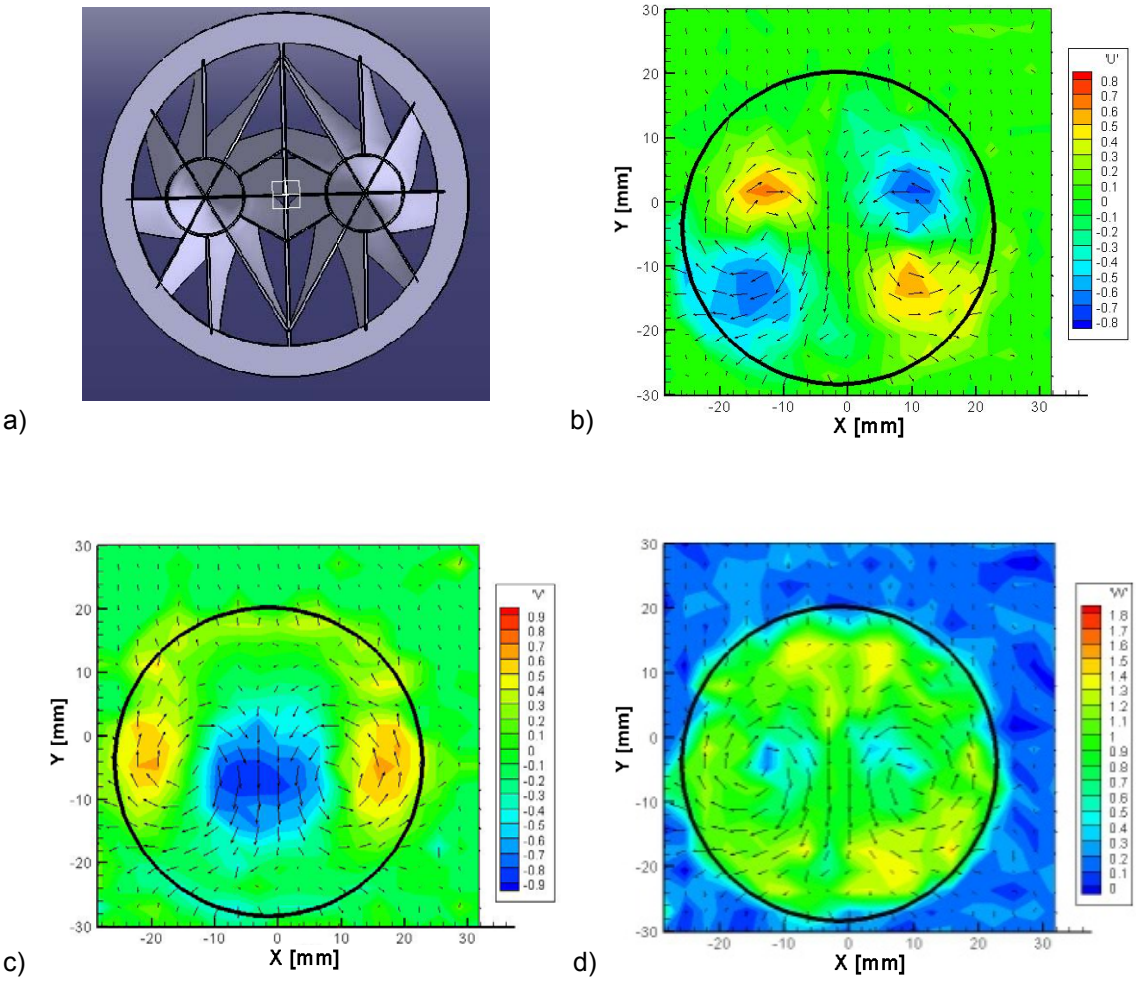

Figure 3.3 Contour of velocity vector fields for Models 2 a) Axial view from inlet side, b) lateral velocity, u, c) vertical velocity, v, d) axial velocity, w

3.2.3 Model #3 (M-3)

This model was identical to M-1 with the exception that the vane twist was removed and the vanes were canted at angles consistent with the maximum swirl angle of 45 degrees at the solid body/potential flow intersection. Because the vanes are canted at high angles in this region, some local flow separation was

anticipated in this region. Results from flow mapping (Figure. 3.4) reveal large variations in axial velocity. Axial flow is reduced in the solid body region and increased near the periphery (particularly at the top and bottom) of the device. The effective resistance of the 6 vane arrangement in the solid body region was implicated as a potential explanation for this behavior. Transverse velocities were reduced in magnitude as compared to the theoretical values.

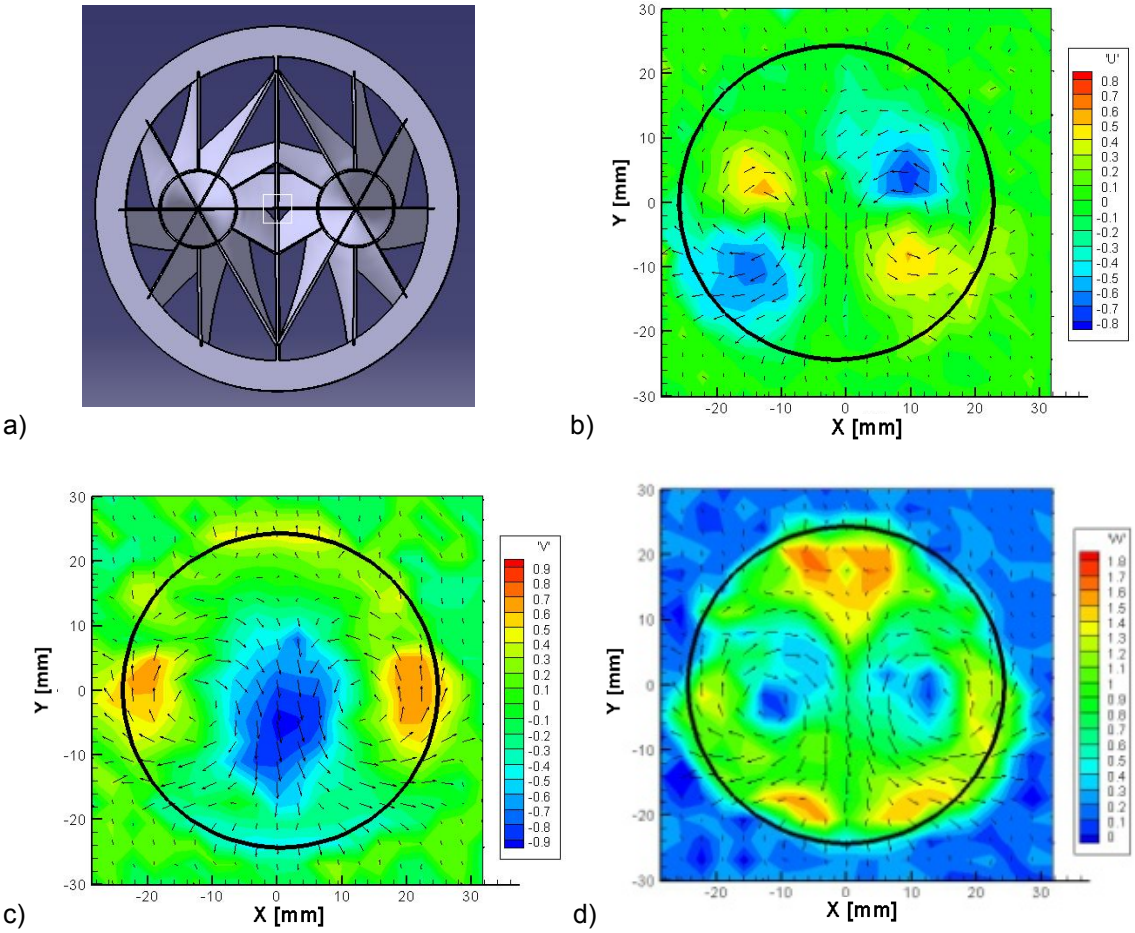

Figure 3.4 Contour of velocity vector fields for Models 3 a) Axial view from inlet side, b) lateral velocity, u, c) vertical velocity, v, d) axial velocity, w

3.2.4 Model #4 (M-4)

To improve flow through the vortex centers, M-4 was designed to have two vanes in the Rankine vortex rather than 6 as used in the prior designs. Figure 3.5 highlights results from this design. In comparison with M-3, M-4 did show more axial flow near the vortex centers, but still displayed some evidence of higher axial velocities near the top and bottom of the device. Transverse velocities were comparable to those in the prior designs M-1, M-2, and M-3.

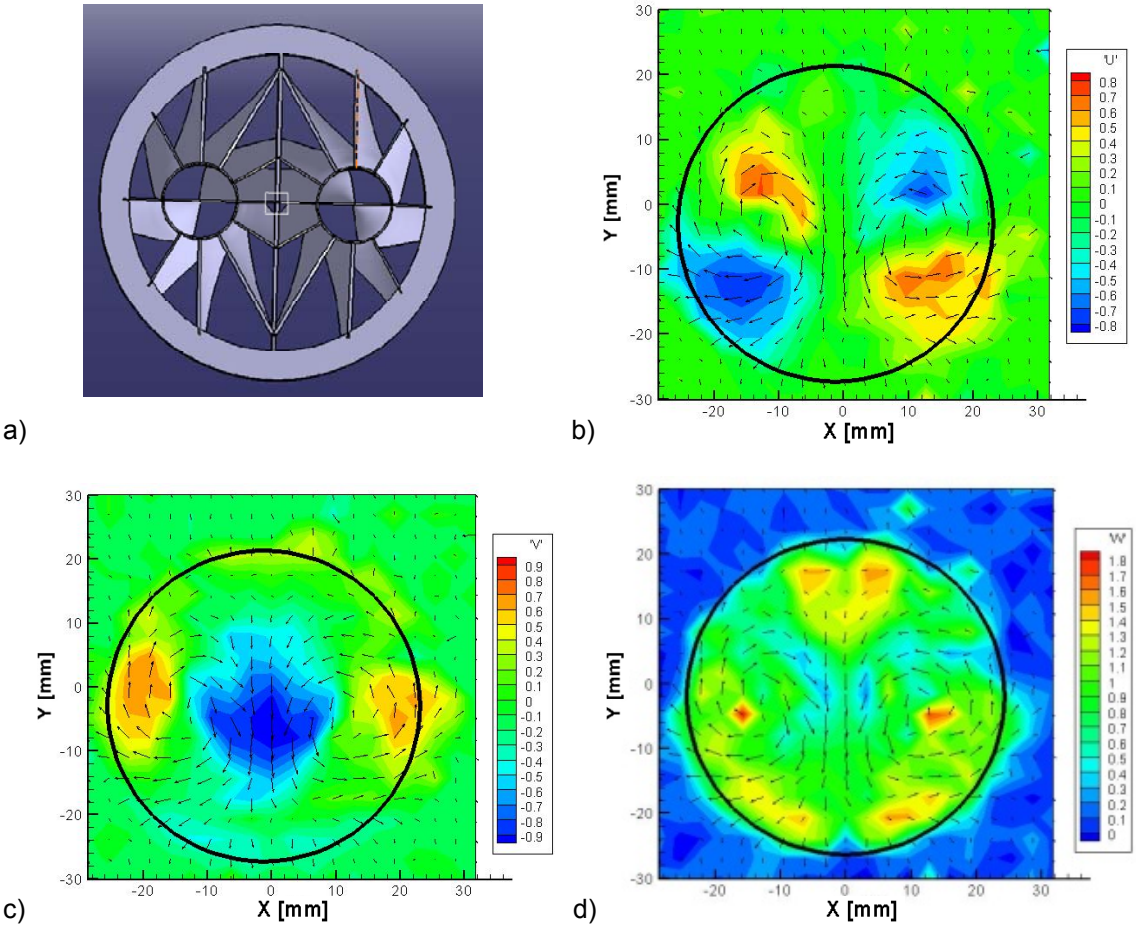

Figure 3.5 Contour of velocity vector fields for Models 4 a) Axial view from inlet side, b) lateral velocity, u, c) vertical velocity, v, d) axial velocity, w

3.2.5 Model #5 (M-5)

M-5 is developed to study the effect of R_s, using an increased value to permit a more gradual transition from solid body to potential vortex rotation. Physically, this is a rather subtle change, but more vane twist is evident (as compared to M-4) in the two vanes within the solid body rotation region. Figure 3.6 summarizes the outlet flowfield for this design. Overall performance was poor relative to the earlier models as less flow is swirled by potential vortices and more by solid body rotation in this scheme. High axial flow nonuniformity was also present. For this reason, we returned to R_s values used in prior designs for most of the subsequent models.

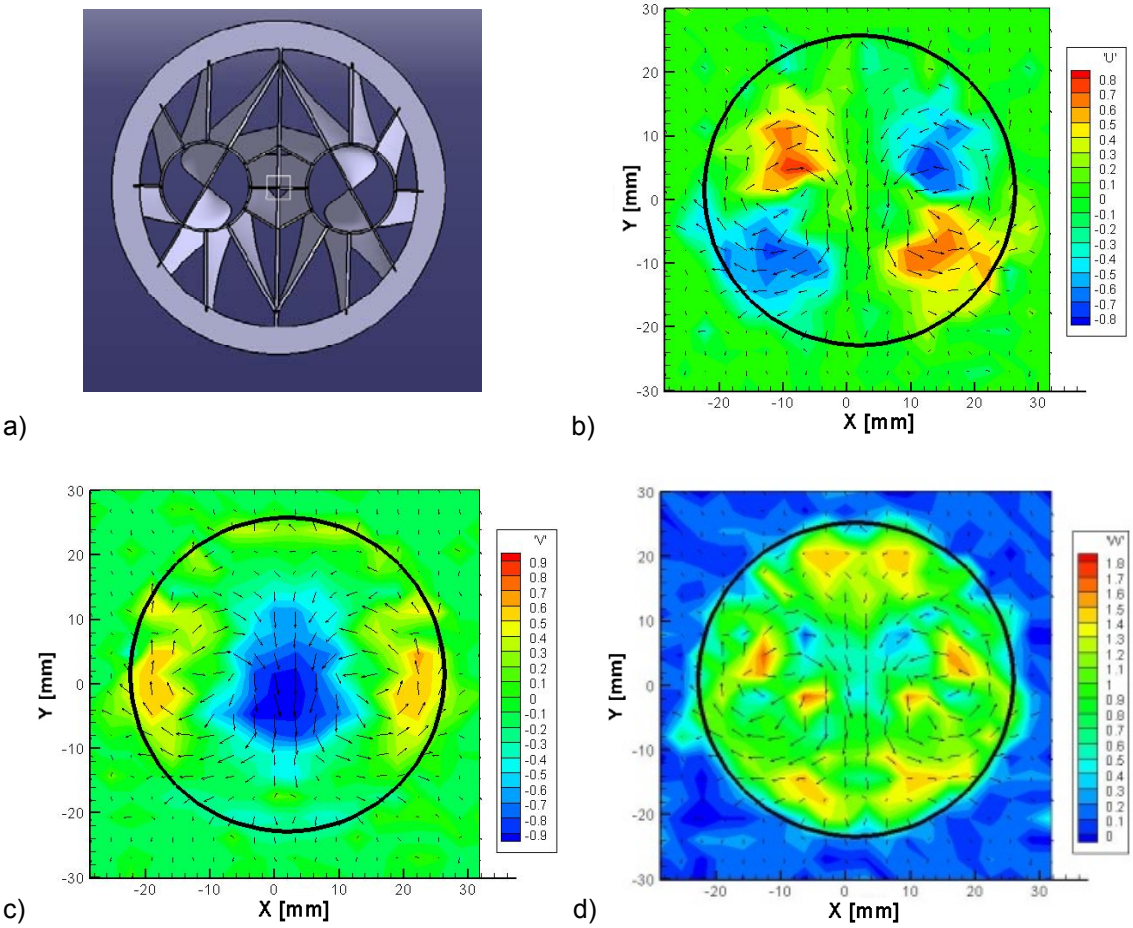

Figure 3.6 Contour of velocity vector fields for Models 5 a) Axial view from inlet side, b) lateral velocity, u, c) vertical velocity, v, d) axial velocity, w

3.2.6 Model #6 (M-6)

Models 1-5 all show substantial non-uniformity in axial flow velocities due to the sparseness of vanes at the very top and bottom of the swirler. The vane arrangement in these regions was modified in M-6 in order to create a more uniform cross-sectional area between successive vanes. For M-6, the vanes of located at 120, 150 and 180 degree are shifted to 110, 130 and 170 degree., Other than this change, the design was identical to M-4. Figure 3.7 depicts measured results; Transverse velocities and axial velocity uniformity were similar

to those of other prior designs. It was unclear to define distinctions between M-5 and M-6 with respect to their performances.

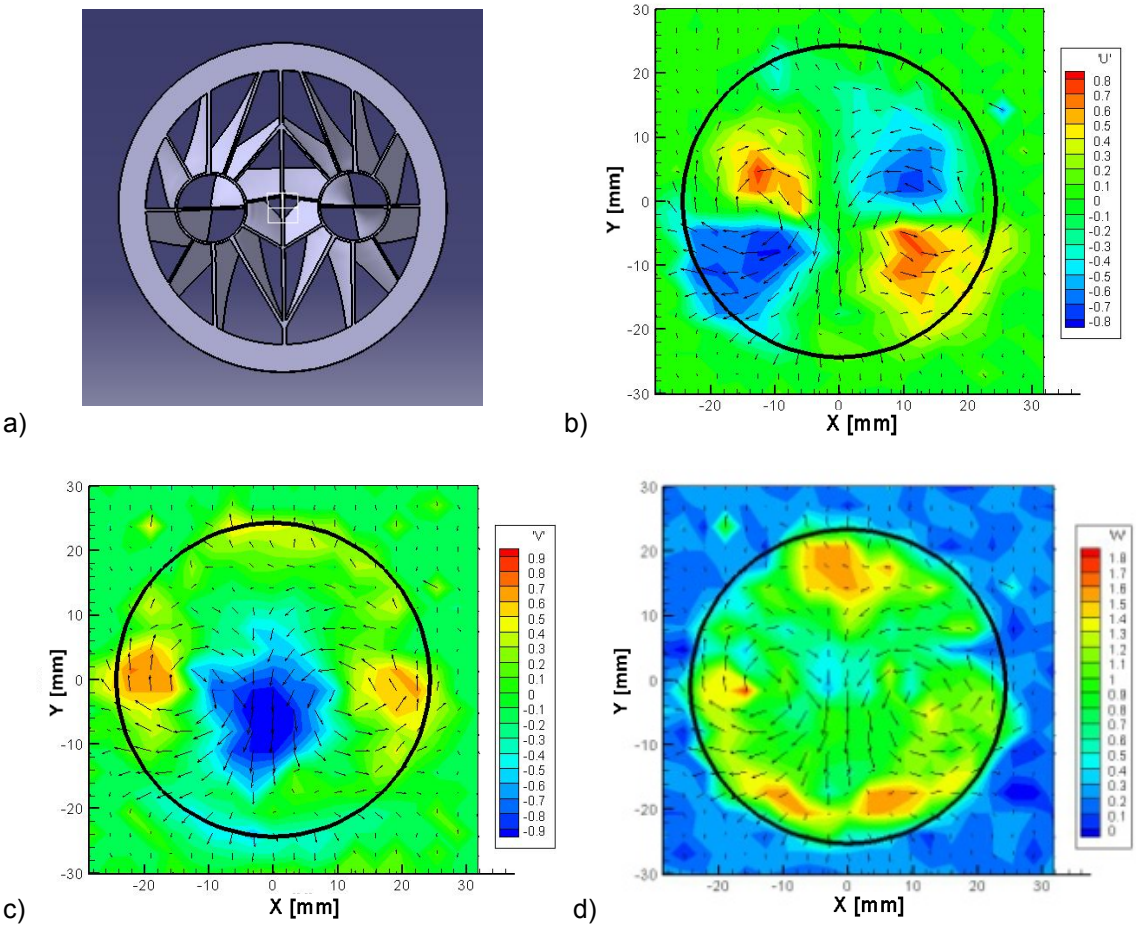

Figure 3.7 Contour of velocity vector fields for Models 6 a) Axial view from inlet side, b) lateral velocity, u, c) vertical velocity, v, d) axial velocity, w

3.2.7 Model #7 (M-7)

Model M-7 was designed to assess the effect of a smaller ring support (R_s) compared to the performance of the M-6. The ring has a 3.6 mm radius with the same potential flow vane arrangement as M-6. With the reduced R_s, vanes were eliminated near the vortex centers. Figure 3.8 highlights the overall flowfield measured at the swirler exit. The increased length of the potential flow vanes

produced stronger transverse velocities as compared to prior models. However, there was little space for the air to flow around the vortex center due to the finite thickness of the vanes and a region of low axial flow was observed between the two vortex centers. Similar to other designs, high axial velocities were measured at the top and bottom of the device.

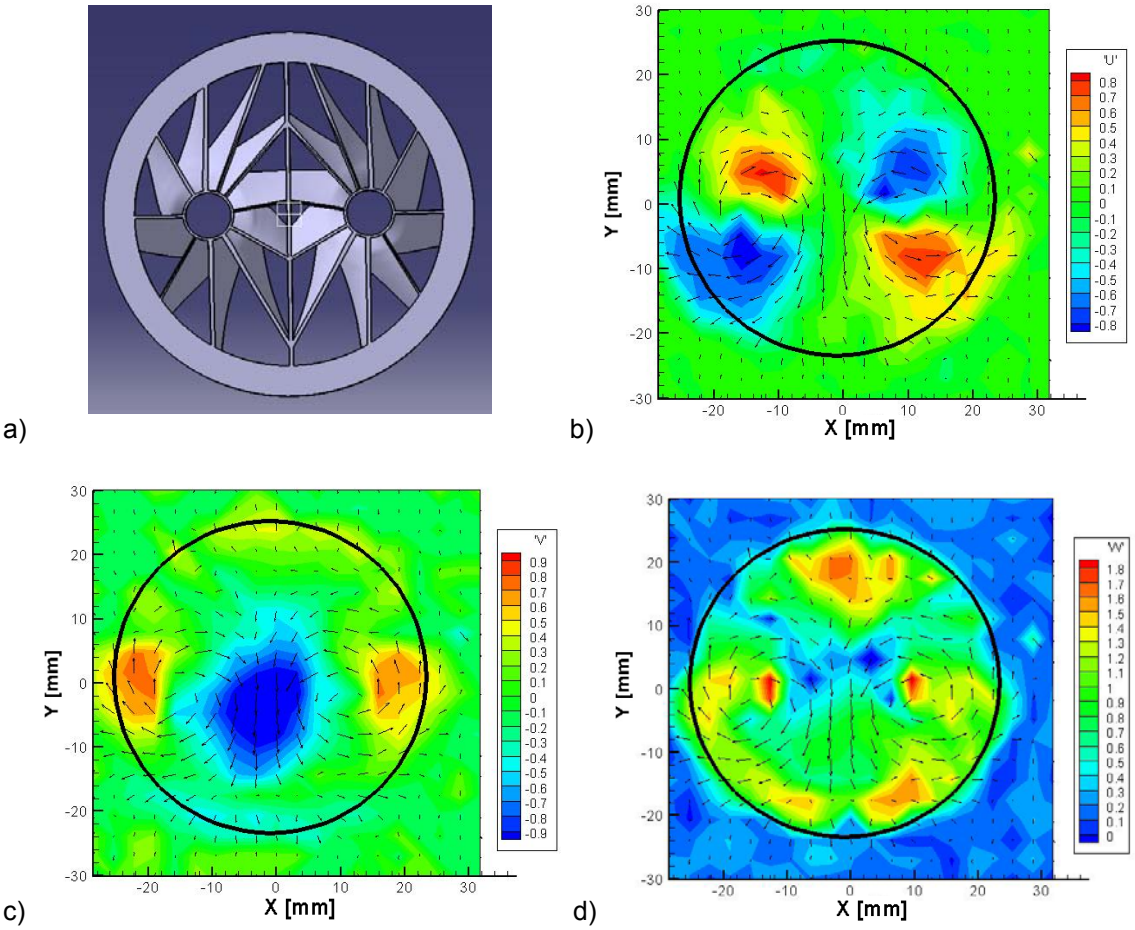

Figure 3.8 Contour of velocity vector fields for Models 7 a) Axial view from inlet side, b) lateral velocity, u, c) vertical velocity, v, d) axial velocity, w

3.2.8 Model #8 (M-8)

Model M-8 was constructed to explore alternate vane arrangement to improve axial flow uniformity, and increase transverse velocities. The model was identical to M-3 with the exception of the new vane arrangement with zero vanes in the vortex center region and shifted vane locations in the potential flow region as highlighted in Table 3.1. Elimination of vanes near the vortex centers proved to be a poor idea as large axial flow was observed (Figure 3.9) in this region due to the reduction in flow resistance.

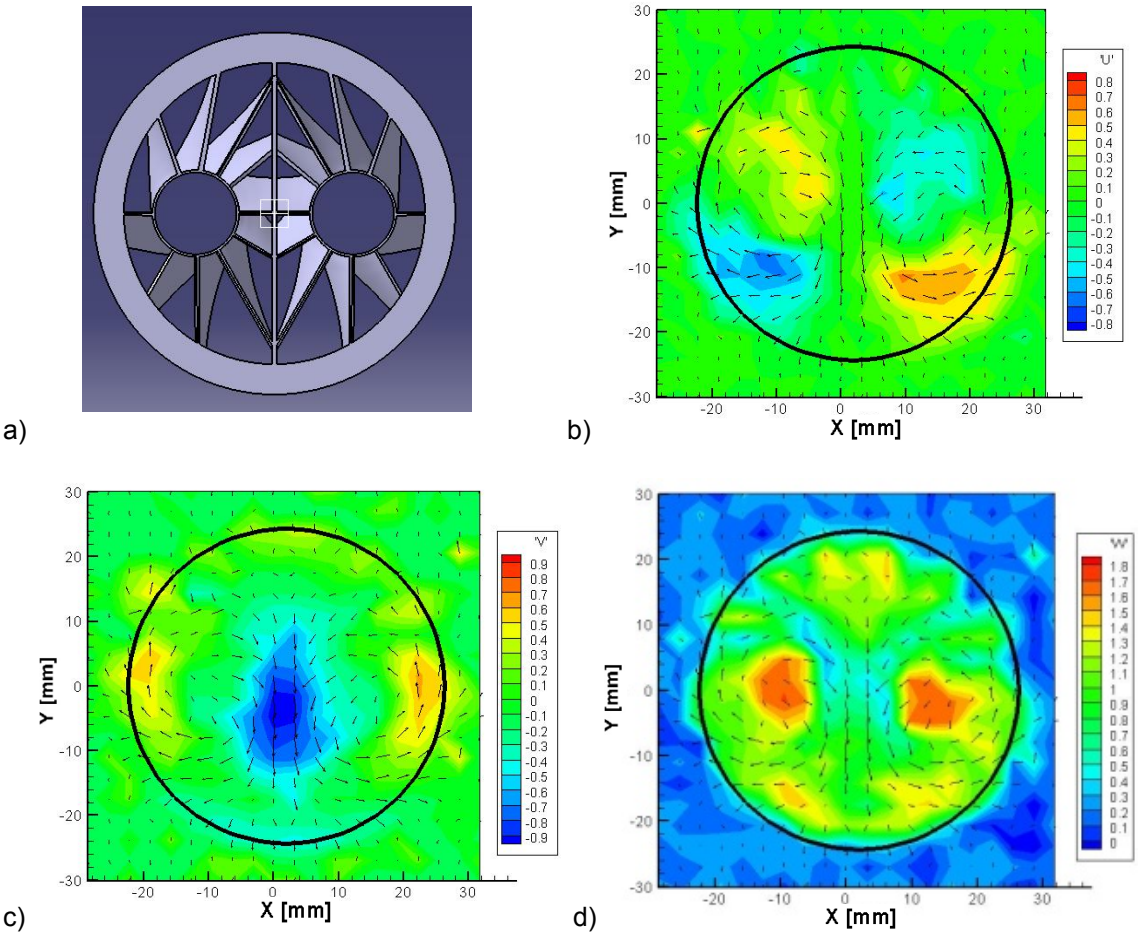

Figure 3.9 Contour of velocity vector fields for Models 8 a) Axial view from inlet side, b) lateral velocity, u, c) vertical velocity, v, d) axial velocity, w

3.2.9 Model #9 (M-9)

M-9 was developed to have the same vane arrangement as that of M-8 with two vanes in the vortex center region to better balance local flow resistance across the entire surface of the device. Figure 3.10 displays resultant exit flow field for this design. This model produced strong tangential velocities over extended areas and exhibited improved axial flow uniformity as compared to prior designs. In particular, the lateral (u) velocities produced by this design were the largest observed among the models discussed to this point. It is interesting to note that the lateral velocities are higher in regions below the vortex centers than those above the vortex centers. The tendency for the vortices to move downward as one travels downstream from the swirler exit is quite evident in this design.

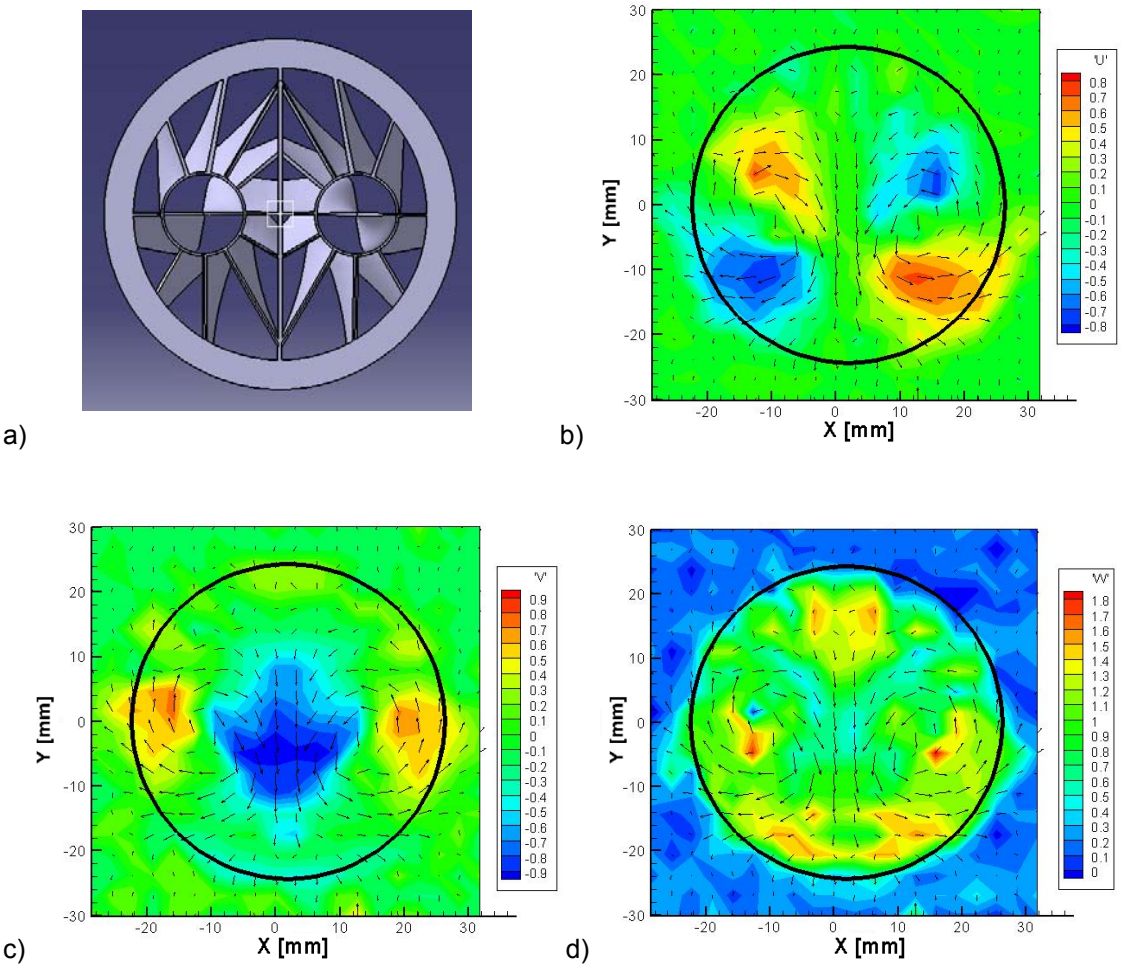

Figure 3.10 Contour of velocity vector fields for M-9 a) Axial view from inlet side, b) lateral velocity, u, c) vertical velocity, v, d) axial velocity, w

Because M-9 produced enhanced transverse velocities with reasonable uniformity in axial velocity, additional flow characteristics were explored for this design. The contours of measured u and v are compared with theoretical data in Figure 3.11. Lateral velocities comparable to analytic results are obtained with the M-9 design. As discussed previously, higher velocities are measured below the vortex centers as compared to those above the vortex centers. Even though the profiles are measured a distance of 0.5 inches (1.25 cm) downstream of the

exit, it is apparent that the vortices have moved downward somewhat in this short distance. Peak u velocities occur about 6 mm below the vortex centers in the analytic results as compared to 10 mm for the measured results, i.e. the vortices have moved downward approximately 4 mm in the 12.5 mm distance from the swirler exit to the measurement location.

The vertical velocities produced by M-9 are also comparable to the theoretical values in Figure 3.12. The large downward flow between the vortices is enhanced in the measured data, likely due to downward motion of the vortices at the point where the measurements are taken. Upward velocities at the periphery of the mixer plane are suppressed somewhat when compared to theory for the same reason.

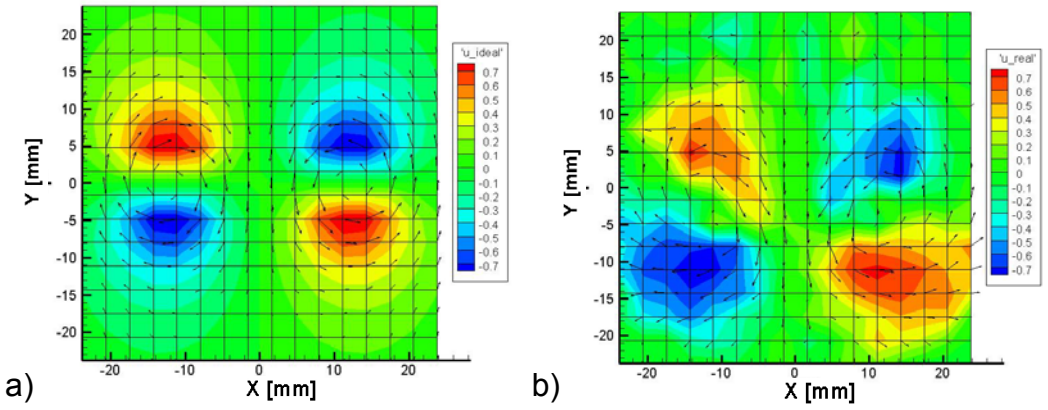

Figure 3.11 a) Theoretical and b) measured lateral velocity fields, u, of Model 9

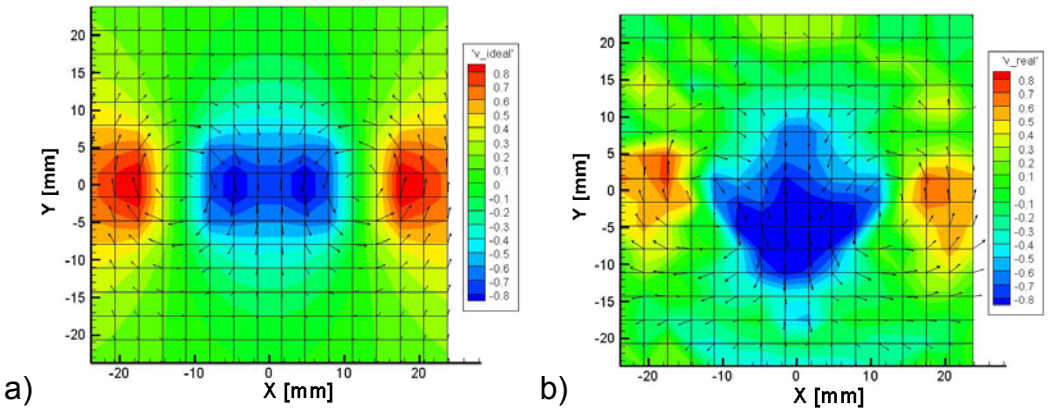

Figure 3.12 a) Theoretical and b) measured vertical velocity fields, v, of Model 9

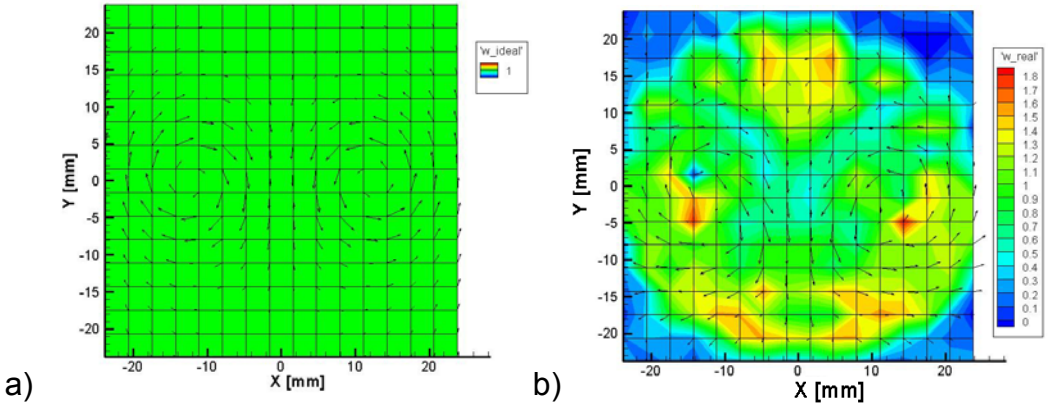

Figure 3.13 a) Theoretical and b) measured axial velocity fields, w, of Model 9

Figure 3.13 compares axial velocities from the device. Theoretically, uniform axial velocity is obtained (neglecting frictional and flow separation effects). Local nonuniformities exist, but overall the measurements show good uniformity in axial velocity.

3.2.10 Flowfield Evolution: Injection into Stagnant Air

To evaluation flow evolution and mixing, a detailed survey was conducted one diameter from the exit of the CVP swirler using the M-9 design. A finer mesh, (35 by 35 with a 0.0625" (1.59 mm) step size) was employed for this survey. Figure 3.14 provides results from these measurements.

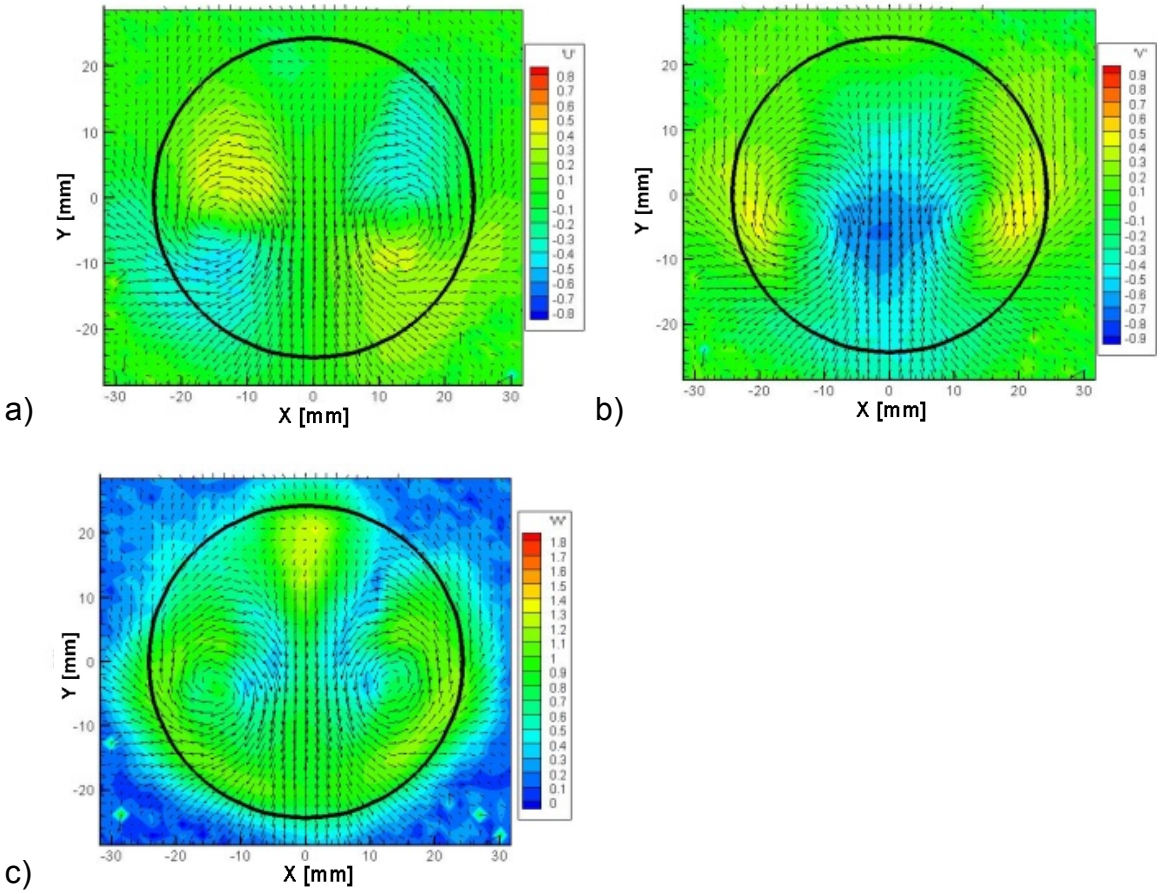

a) Lateral velocity, u b) Vertical velocity, v c) Axial velocity, w

Figure 3.14 Contour of Velocity components for Model 9, 1-D Downstream of Injection into Ambient Air

The results show vertically downward motion of the vortex centers from Y=0 mm at the exit plane to Y= -5 mm (-0.2") in the survey one diameter downstream from

the exit. Axial and transverse velocities have dropped significantly and there is strong evidence of entrainment of low-energy ambient air toward the vortex centers. The jet has broadened vertically, particularly on its lower side, as well as horizontally in the region near the centerline connecting the vortices.

3.2.11 Flowfield Evolution: Injection into Pipe

As a potential near-term application for the mixer is to enhance performance of hybrid rocket combustion, a survey was conducted downstream of the mixer exit, but still inside the cylindrical duct. A 2”/50.8 mm (one diameter long) pipe section was fastened to the downstream side of the mixer and a survey was taken at the exit of this pipe. Figure 3.15 reveals that substantially higher transverse and axial velocities were measured in this case as compared to the injection into stagnant air (Figure 3.14). Since the flow is not mixing with low-energy ambient fluid in this case, the degradation in velocities is attributed solely to viscous effects. Some degradation is noted if one compares results with the survey near the mixer exit plane (Figure 3.10). Another interesting aspect of this internal flow is that the vortex centers do not appreciably translate vertically. There is some evidence of rotation of the vortex centers, i.e. the vortex on the right shifts upward slightly while the one on the left is shifted downward very slightly.

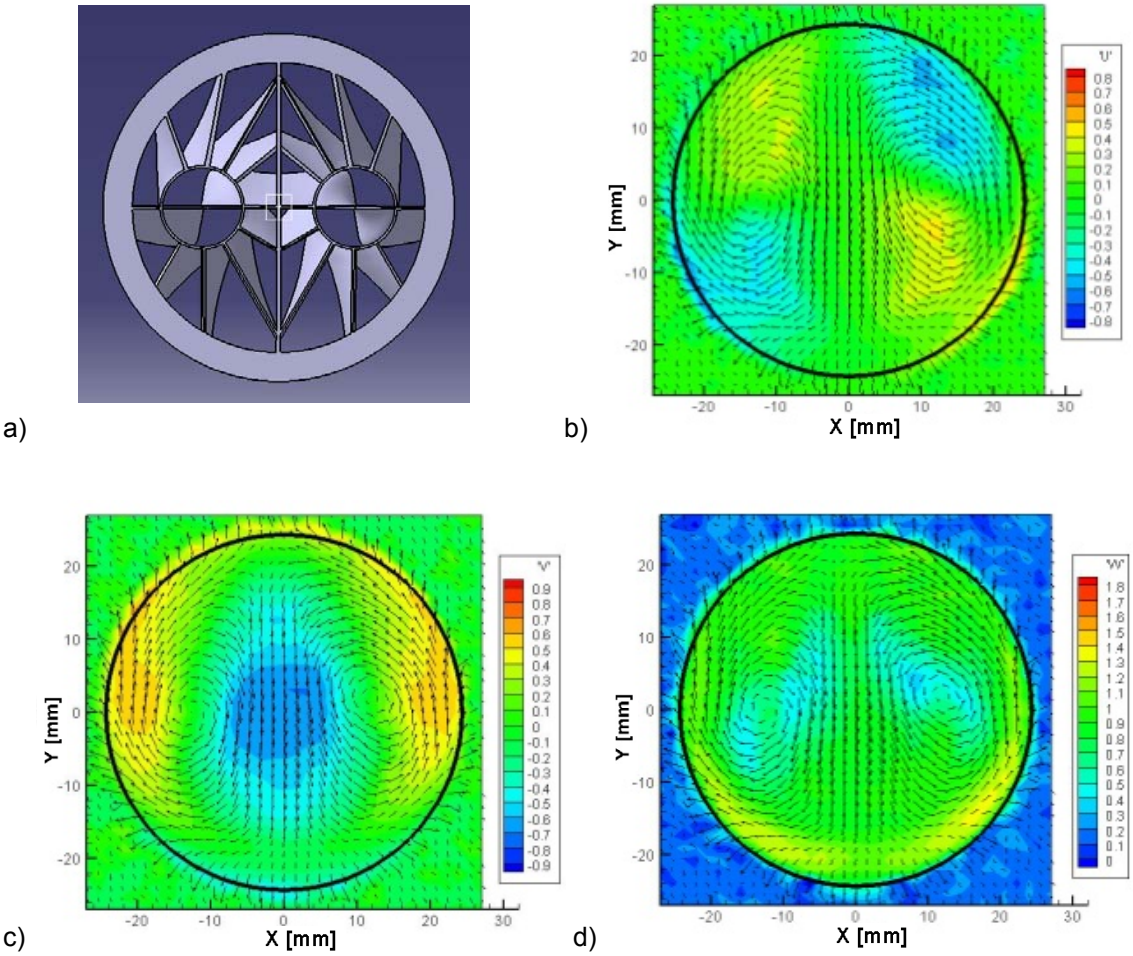

Figure 3.15 Velocity vector fields in a pipe one diameter downstream of M-9 model a) CAD drawing, b) lateral velocity, u, c) vertical velocity, v, d) axial velocity, w

3.2.12 Optimization (Models M-10, M-11, M-12)

The M-9 mixer design provides characteristics that we seek in that large transverse velocities are created, while nearly uniform axial flow is maintained. However, locally high axial velocities were still apparent near the bottom of the device as highlighted in Figure. 3.15d for a measurement 1D downstream of the exit. To resolve this problem, the vane arrangement was altered in M-10 as

described in Table 3.1. Model M-11 was also developed to address this problem by incorporating an additional vane at the bottom of each vortex center.

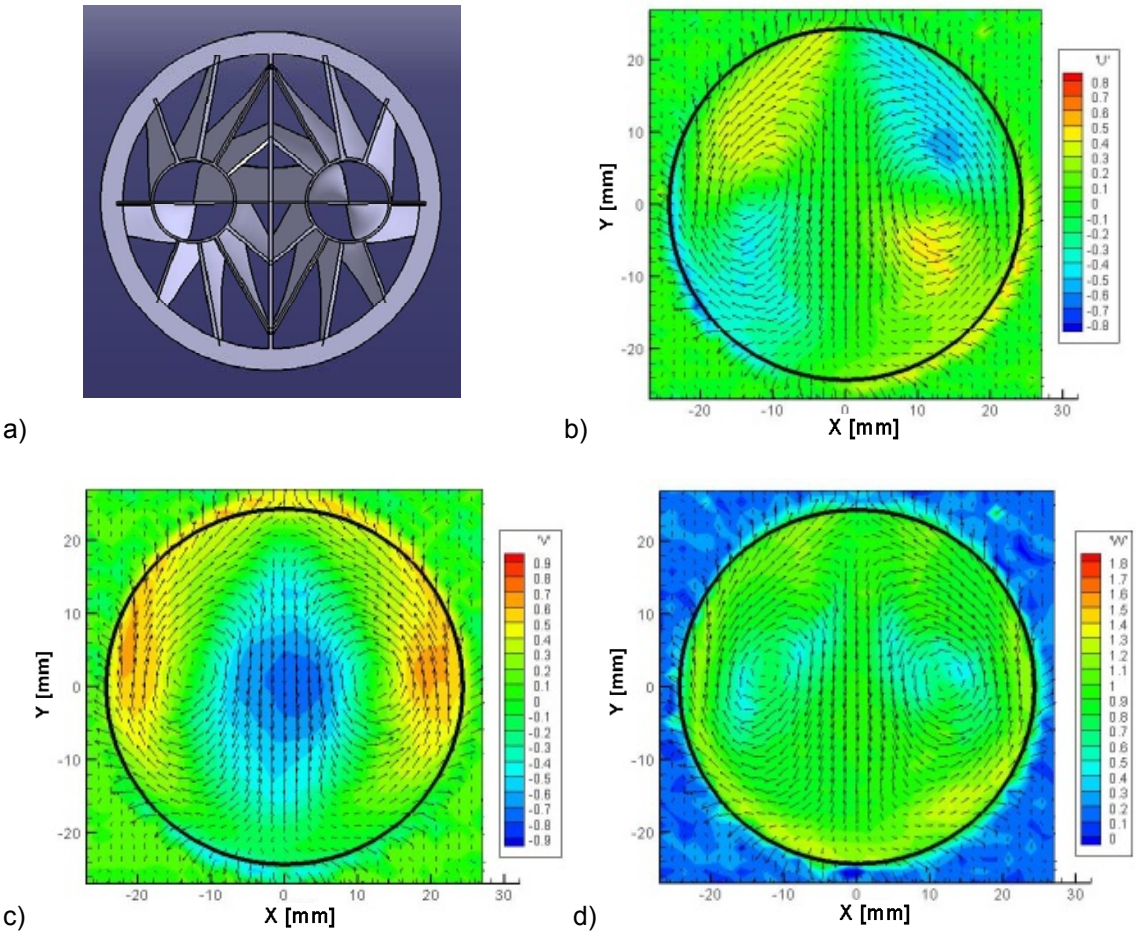

Figure 3.16 Velocity vector fields within a pipe for M-10 one diameter downstream of exit a) CAD drawing, b) lateral velocity, u, c) vertical velocity, v, d) axial velocity, w

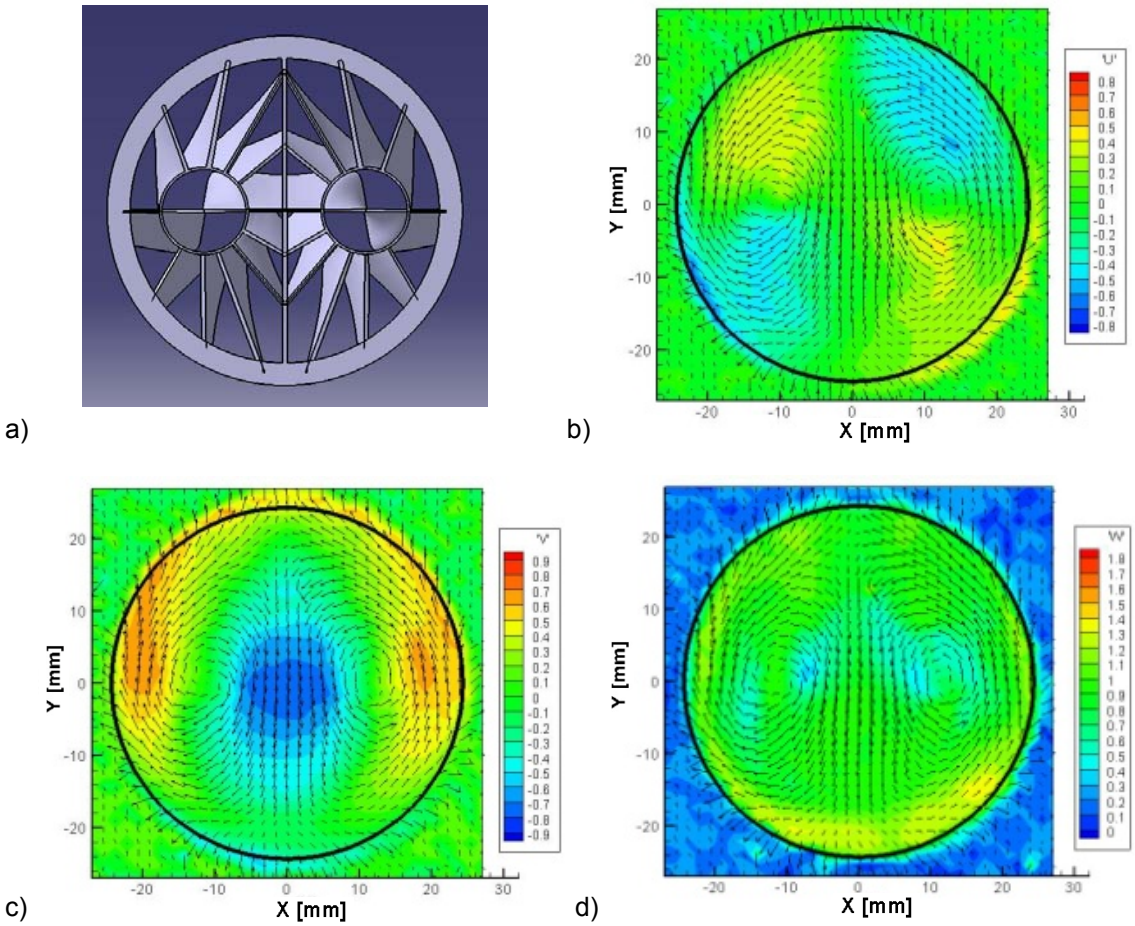

Figure 3.17 Velocity vector fields for M-11 measured within a pipe one diameter downstream of mixer exit a) CAD drawing, b) lateral velocity, u, c) vertical velocity, v, d) axial velocity, w

Figure 3.16 and Figure 3.17 show the velocity fields from M-10 and M-11 respectively. The results from the M-10 were encouraging in that the swirl velocities became more intense than M-9, while the axial velocity was more uniform in the region near the bottom of the device. However, for M-11 it turned out that adding one more vane did not improve results significantly.

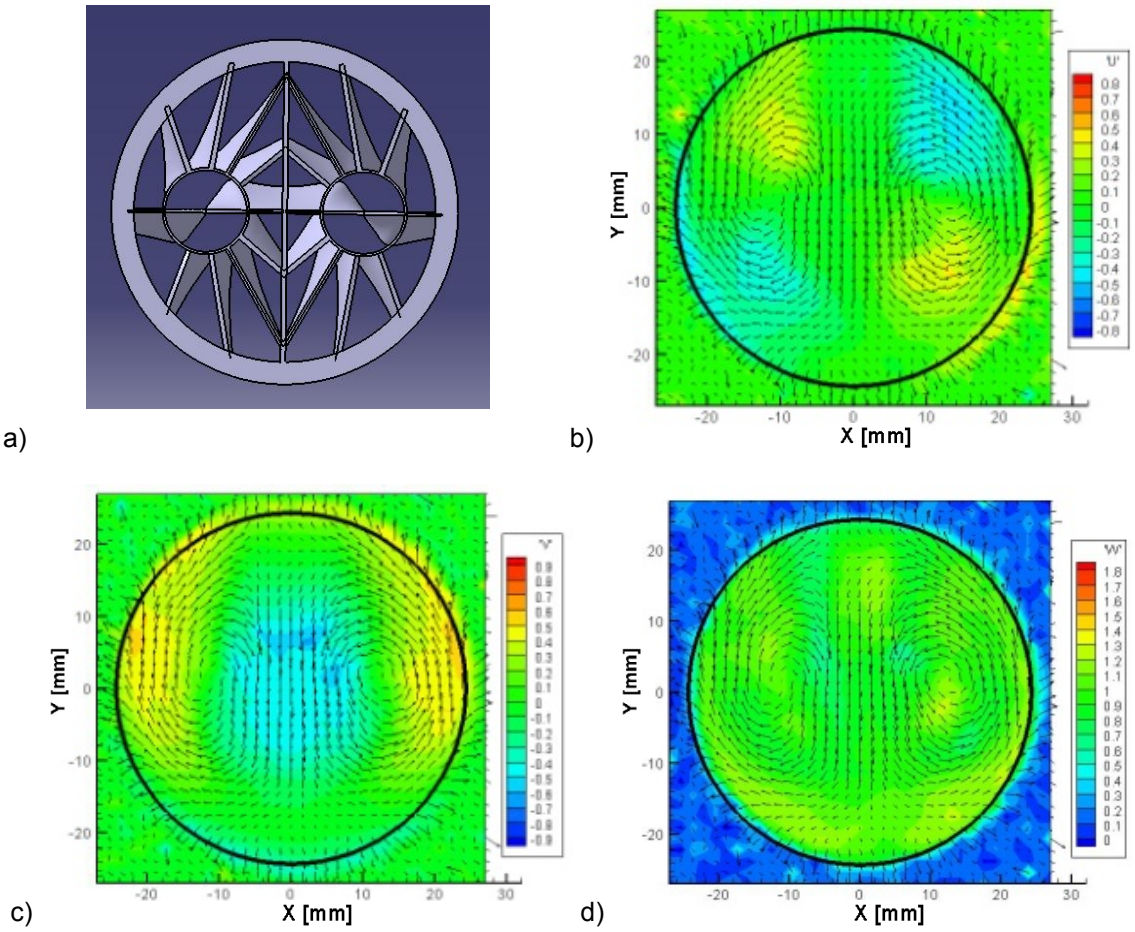

Figure 3.18 Velocity vector fields of the Model 12 with a pipe a) CAD drawing, b) lateral velocity, u, c) vertical velocity, v, d) axial velocity, w

Model M-12 was created to assess lower swirl levels. It incorporated the same design of the M-10 except the maximum vane angle at r=R was reduced from 45 degrees to 30 degrees. The results show consistently weaker transverse velocities as evidenced in Figure. 3.18. Uniformity of axial flow is excellent and the peak transverse velocities are comparable to those predicted from the analytic model. The design variables used on Model M-10 appear to be the most attractive from the units investigated. The vane arrangement provides excellent swirl and uniform axial flow over a the two swirl levels investigated.

3.2.13 Flow Evolution in Pipe for Model M-10

To study evolution of the the counter rotating vortices as they proceed downstream within a pipe, flow fields by M-10 were surveyed at one, three and five diameters away from the exit plane. The contours in Figure 3.19 have a different scale of legends compared to previous results in order to see the distance effects clearly. As shown in Figure. 3.20, the intensity of the tangential velocity decreased but the axial flow became uniform as the vortices proceed downstream. There is evidence of some rotation of the vortices as was observed in similar survey with M-9 (Figure 3.15). At the 5D distance, there is also evidence of some bulk downward motion of the vortices. It would be interesting to see if these structures persist in larger Reynolds numbers in longer pipes.

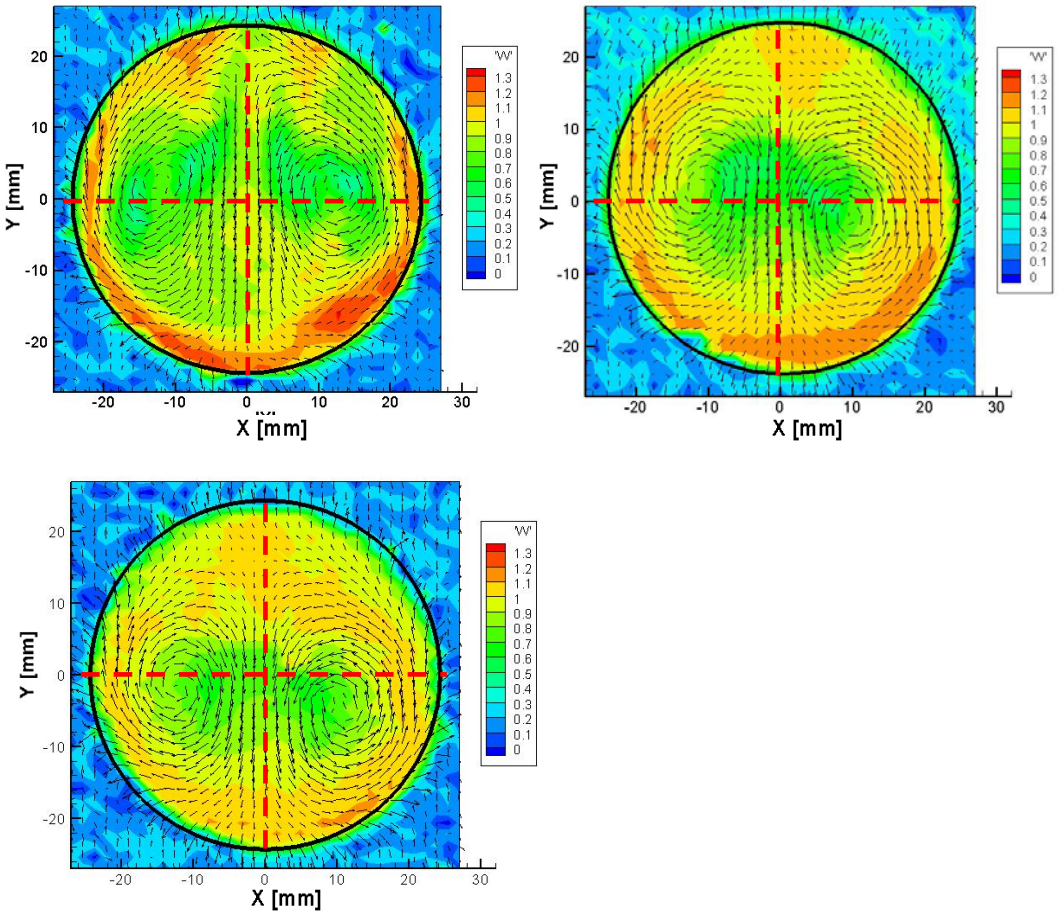

Figure 3.19 Effects of distance on flowfield a) at one diameter distance, b) at three diameter distance, c) at five diameter distance from mixer exit plane

Finally, Figure 3.20 provides detailed measurements for transverse velocities for each of the three downstream locations noted in Figure 3.19.

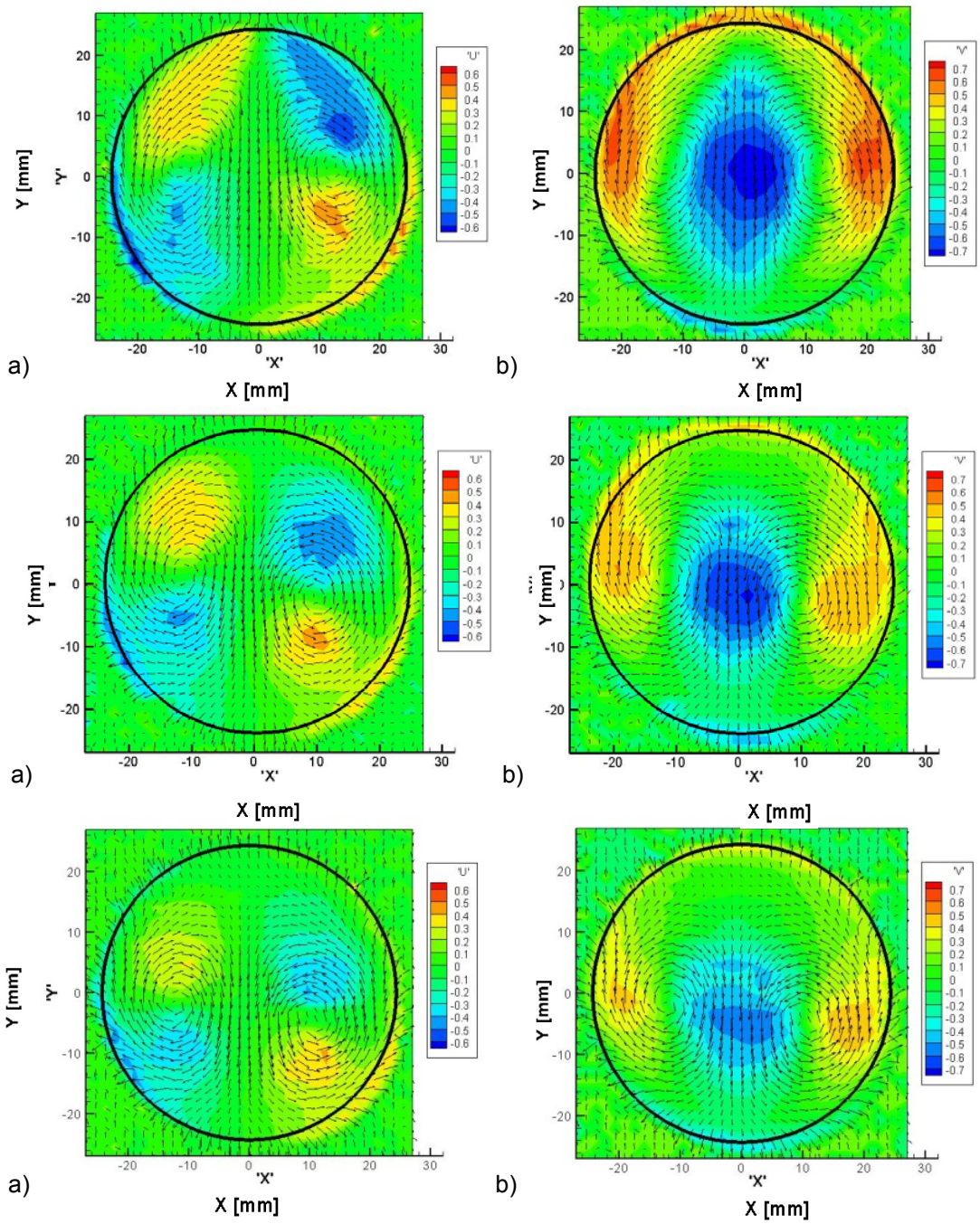

Figure 3.20 Contours of a) lateral velocity, u, b) vertical velocity, v. From top to bottom at one diameter, three diameter, and five diameter downstream

3.2.14 Static Pressure Drops by a CVP Mixer

Static pressure drops due to the mixer configurations were measured in a hybrid rocket test rig at MLZ. The experimental setup has been developed to estimate the effects of various fuels with pure oxygen gas flows on the hybrid motor performances. For static pressure drop measurement, pressurized nitrogen gas is supplied instead of the pure oxygen gas. A 2” PVC pipe is adapted to the chamber as shown in Figure 3.21, and thereby the pressure drops are attributed solely to the mixer configurations. The details about the hybrid rocket test rig can be found at the reference[21].

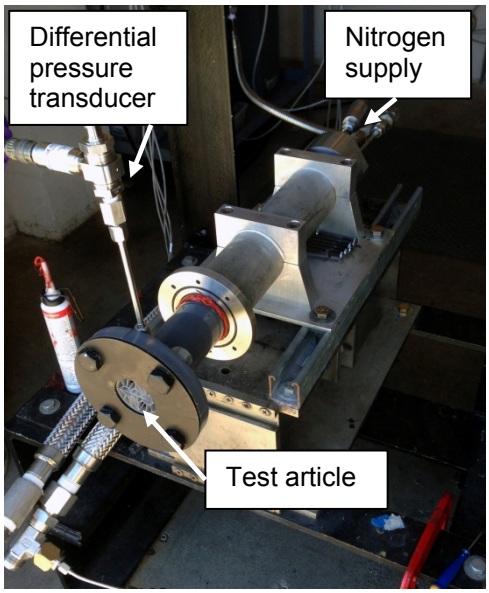

Figure 3.21 Test rig for static pressure drop measurement

The pressure drops were assessed for the metal mixers (M-13 and M-14) over a range of mass flow rates applied across the inlet and outlet of the test article. The mass flow rates were measured by a sonic venturi and varied from 0.3 lbm/s to 0.6 lbm/s. In Figure 3.22, the pressure drop showed a trend of quadratic curves

as fluid resistance is proportional to the square of the velocity. M-13 caused 0.39 psi pressure drop at the maximum flow condition and 0.08 psi for M-14. In a hybrid rocket application, the pressure drops by both mixers can be thought to be very small as compared to those by other factors in the engine. The measured data were also analyzed across dynamic pressures to evaluate loss coefficients of the metal CVP mixers. This is useful parameter to estimate pressure losses by the mixer with variation of flow conditions. The loss coefficient, *K* is defined as $\mathrm{dP} = K\mathrm{q}$, where dP is static pressure drop and q is dynamic pressure. M-13 and M-14 had loss coefficients of 0.0105 and 0.0024 respectively as shown in Figure 3.23.

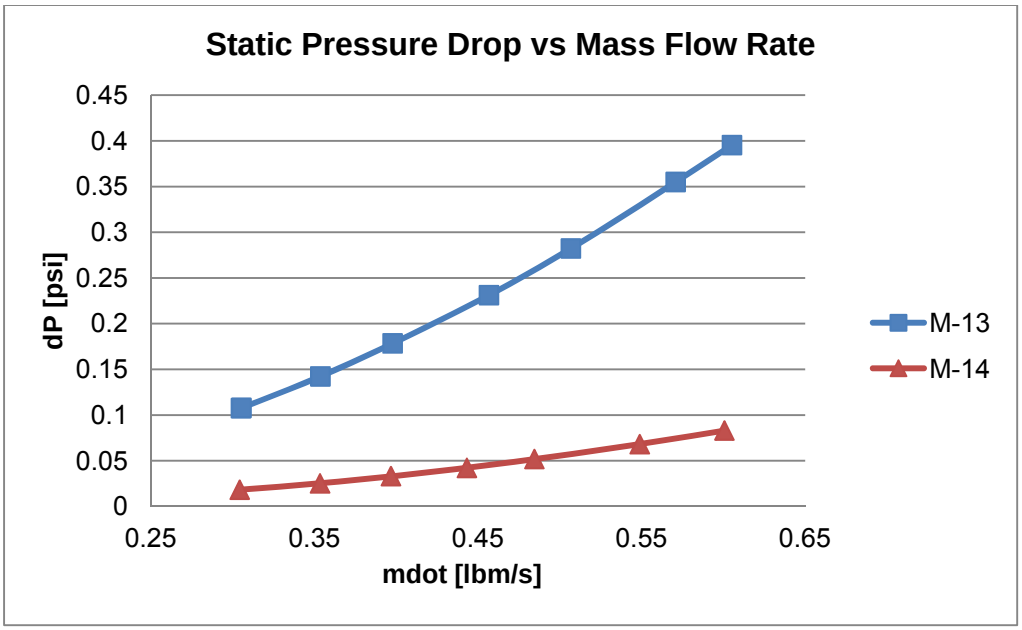

Figure 3.22 Estimated static pressure drops across mass flow rates

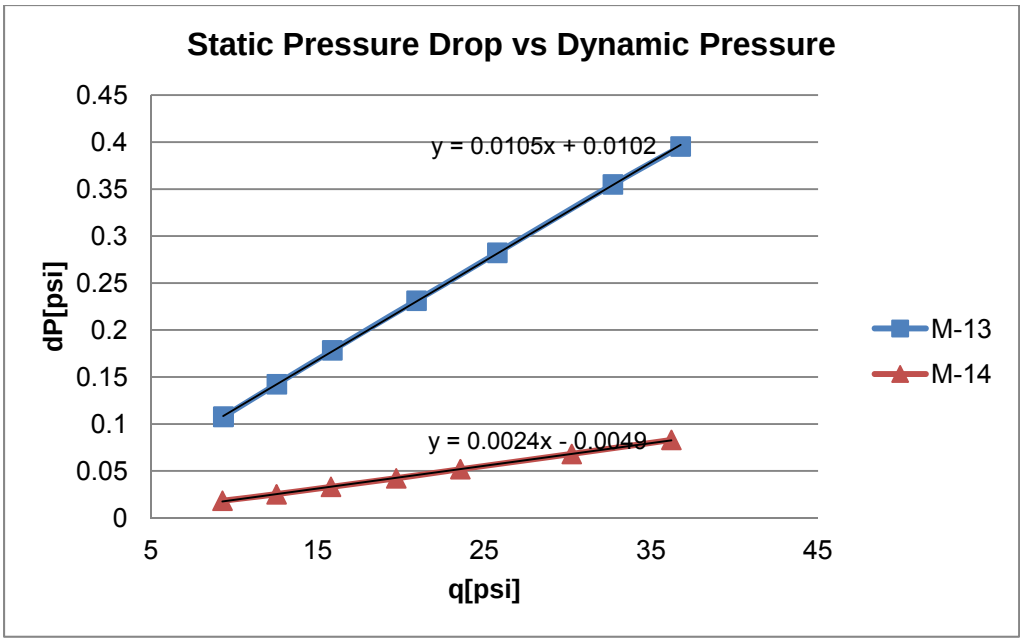

Figure 3.23 Estimated static pressure drops across dynamic pressures

CHAPTER 4. CONCLUSIONS AND RECOMMENDATIONS FOR FUTURE WORK

4.1 Conclusions

A counter rotating vortex pair mixer design has been proposed based on the potential theory. Milne-Thomson's Circle Theorem constrains the vortex pair to place within a cylindrical tube and Rankine vortex was applied to remove the singularity at the vortex center. An ideal velocity vector fields was generated by the analytic analysis. With the analytic data, streamlines were computed and vane surfaces were generated with a series of the streamlines along the vane leading edges, thereby creating vanes by giving a thickness on the surfaces. Measurements have been obtained for fifteen different test models printed by a 3D printer or DSML technology, with variations of design variables using the setup. The results showed qualitative counter rotating swirling behaviors matching very well the theoretical results. Based on the results, Model 10 reproduced velocity vector fields best. In addition, the DSLM technology has been utilized to manufacture the highly complex geometry of the CVP mixers (M-13 and M-15) with Inconel 718.

Vanes with immediate turning to angle α_{max} were chosen over designs than with gradually increasing angles and a shorter length of the vane length (L), 1/3", was preferred for designs. In addition, additional vanes more than ten did not provide an advantage on axial flow uniformity. With respect to vane arrangements, some of the vanes must be located in the upper and lower dead zones, such as 100, 120, 240 and 260 degree from each vortex center, so that the CVP mixer provides a balance of complexity and blockage introduced by the vanes with the desired flow field turning intended by the design.

As flow proceed downstream, the low energy ambient air were entrained toward the vortex centers, which implies potential of better mixing by the entrainments. In addition, the vortex centers were moved vertically downward by induced forces from each vortex. Interestingly, the case of the flow was constrained within a cylindrical duct, vortex centers began to rotate as the downward motion was restricted by the cylindrical solid boundary.

The CVP mixers made of Inconnel 718 was evaluated with respect to pressure drop characteristics. The pressure drops were small enough to be applied to hybrid rocket engines. Gross mixing performance under hotfire conditions and the results will be reported in the near future by Steven Shark[21].

4.2 Future work

The injection of a round jet into crossflow is a classical three-dimensional flowfield that is important in propulsion systems. The jet in crossflow is composed of a series of inter-related vortex systems, as shown in the sketch in Figure 4.1.

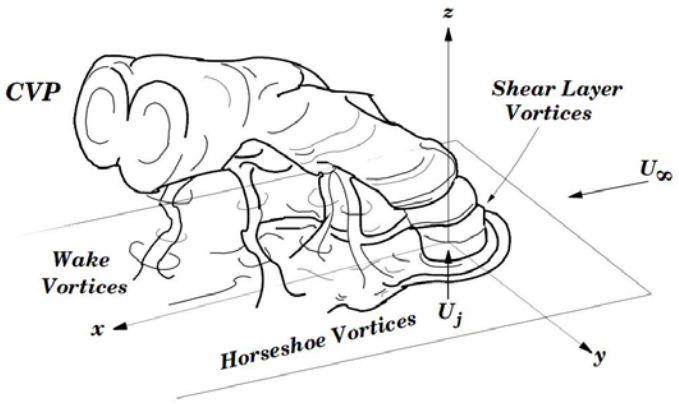

Figure 4.1 Schematic of the transverse jet, introduced ush with respect to the injection wall, and relevant vertical structures[20]

In the far-field of the jet structure, the counter rotating vortex pair (CVP) is dominant, which are believed to be primarily responsible for the enhanced mixing. This implies that it has potential to improve the mixing further if the jet structure possesses the CVP from its near-field generation. The CVP mixer presented in this thesis has a capability of generating the counter rotating vortex pair flow immediately. Therefore, one of interesting future works will include injection of a counter rotating “jet” into crossflow by the CVP mixer, thereby investigating the effects of the mixer with respect to the penetration of the jet as well as its mixing with the crossflow fluid.

REFERENCES

REFERENCES

[1] Long, M. B. and Chu, B. T, “Mixing Mechanism and Structure of an Axisymmetric Turbulent Mixing Layer,” AIAA Journal, Vol. 19, NO. 9, Sep. 1981, pp 1158-1163.

[2] McCormic, D. C. and Bennett, J. C. Jr., “Vortical and Turbulent Structure of a Lobed Mixer Free Shear Layer,” AIAA Journal, Vol. 32, No.9, Sep. 1994, pp 1852-1859.

[3] Milne-Thomson, L. M., *Theoretical Aerodynamics*, Dover, Mineola, New York, 1973, pp 84-85.

[4] Tecplot 360, CFD visualization software, Ver. 2012 Amtec Engineering, Bellevue, Washington.

[5] Tecplot User’s Manual, Ver. 10, Amtec Engineering, Bellevue, Washington, 2003.

[6] CATiA, 3D CAD software, Ver. 5R20SP5, Dassault Systems, Waltham, MA.

[7] 5 and 7 Hole Probes Product Manual, Ver. 4.0.0, Aeroprobe Corporation, Blacksburg, VA, 2012.

[8] Tang, “ A Study on the Plume Characteristics and Performance of 2-D Transition Nozzles,” Ph.D Dissertation , School of Aeronautics and Astronautics, Purdue University, Aug. 2008.

[9] Knuth, W. H., Gramer, D. J., Chiaverini, M. J., and Sauer, J. A., “Development and Testing of a Vortex-Driven High Regression Rate Hybrid Rocket Engine,” AIAA Paper 98-3507, Cleveland, OH, 1998.

[10] Yuasa, S, Shimada, O., Imamura, T., Tamura, T., and Yamamoto, K., “A Technique for Improving the Performance of Hybrid Rocket Engines,” AIAA Paper 99-2322, Los Angeles, CA, 1999.

[11] Lilley, D. G., “Annular Vane Swirler Performance,” *Journal of Propulsion and Power*, Vol. 15, No. 2,, Mar. 1999, pp 248-252.

[12] Waitz I.A., Qiu Y.J., Manning T.A., Fung A.K.S., Elliot J.K., Kerwin J.M., Krasnodebski J.K., O'Sullivan M.N., Tew D.E., Greitzer E.M., Marble F.E., Tan C.S., Tillman T.G, “Enhanced Mixing with Streamwise Vorticity,” *Progress in Aerospace Sciences*, Vol. 33, No.5, 1997, pp 323-351.

[13] Tew, D. E., Waitz, I. A., Hermansont J. C., Greitzert E. M. and Tan, C. S. “Streamwise Vorticity Enhanced Compressible Mixing Downstream of Lobed Mixers,” AIAA Paper 95-2746, San Diego, CA , 1995.

[14] Luk, “Experimental Study of Swirling Flows and Mixing in Non-Axisymmetric 2-D Nozzle,” M.S.A.A. Dissertation, School of Aeronautics and Astronautics, Purdue University, May 2010.

[15] Cheng, “Reactive Mixing in Swirling Flows,” AIAA Paper 80-1400, Snowrnass, Colorado, 1980.

[16] Crawford, “Design and Calibration of Seven Hole Probes for Flow Measurement,” M.A.S Dissertation, Department of Mechanical and Materials Engineering, Queen’s University, April 2011.

[17] Gerner, A. A., Maurer C. L. , Gallington R. W., “Non-nulling Seven-Hole Probes for High Angle Flow Measurement,” *Experiment in Fluids*, Vol. 2, Issue. 2, 1984, pp95-103.

[18] Bell, J., “Effects of Streamwise Vorticity Injection on Turbulent Mixing Layer Development,” AIAA Paper 90-1459, Seattle, WA, 1990.

[19] Model 9116 Intelligent Pressure Scanner User’s Manual, Measurement Specialists, Hampton, VA, 2012.

[20] Fric, T. F. and Roshko, A., “Vortical structure in the wake of a transverse jet," *Journal of Fluid Mechanics*, Vol. 279, 1994, pp. 1-47.

[21] *Shark, S. C., Zaseck, C. R., Graham Jr., J.T., Pourpoint, T. L., Son, S. F., and Heister, S. D., “ Visualization and Performance of Hybrid Rocket Solid Fuels in an Optical Cylindrical Combustor,” AIAA Paper 2013-3966, San Jose, CA, 2013.*